

An inverted infall profile for the collapse of the massive star-forming IRDC SDC335.579-0.292

Xie Jinjin (谢津津)^{1,2,3,4}, Gary A. Fuller^{2,5,6}, Di Li (李韵)^{7,3*},
Rowan Smith^{8,2}, Nicolas Peretto⁹, Jingwen Wu⁴, Yongxiong Wang (王永雄)²,
Yan Duan (段言)^{10,3}, Jifeng Xia (夏季风)^{3,4}, Jarken Esimbek^{1,11,4}, Willem A. Baan^{1,12}

¹State Key Laboratory of Radio Astronomy and Technology, Xinjiang Astronomical Observatory, Chinese Academy of Sciences, 150 Science 1-Street, Urumqi, Xinjiang 830000, China

²Jodrell Bank Centre for Astrophysics, Department of Physics & Astronomy, The University of Manchester, Manchester M13 9PL, UK

³National Astronomical Observatories, Chinese Academy of Sciences, A20 Datun Road, Chaoyang District, Beijing 100101, China

⁴University of Chinese Academy of Sciences, Beijing 100049, China

⁵Instituto de Astrofísica de Andalucía (CSIC), Glorieta de la Astronomía s/n E-18008, Granada, Spain

⁶I. Physikalisches Institut, University of Cologne, Zùlpicher Str. 77, 50937 Köln, Germany

⁷New Cornerstone Science Laboratory, Department of Astronomy, Tsinghua University, Beijing 100084, China

⁸SUPA School of Physics and Astronomy, University of St Andrews, North Haugh, St Andrews, Fife, KY17 9SS, UK

⁹School of Physics & Astronomy, Cardiff University, Queen's Building, The Parade, Cardiff, CF24 3AA, UK

¹⁰Space Engineering University, Beijing 101416, China

¹¹Xinjiang Key Laboratory of Radio Astrophysics, Urumqi 830011, China

¹²Netherlands Institute for Radio Astronomy, ASTRON, 7991 PD Dwingeloo, The Netherlands

Accepted XXX. Received YYY; in original form ZZZ

ABSTRACT

There is increasing evidence for global collapse of clumps over parsec-scales in massive star formation regions. Such collapse may result in characteristic molecular line emission profiles but the spatial variation of such lines has rarely been quantitatively examined. Here we explore the infall properties using the spatially-resolved HCO⁺ J=1–0 and H¹³CO⁺ J=1–0 maps of the massive infrared dark cloud (IRDC) SDC335.579-0.292. We compare the observations with the analytical Hill5 model and radiative transfer models. This shows that the best-fit infall velocity towards the cloud centre to be well-constrained to -0.6 to -1.6 km s⁻¹ and the mass infall rate between a few $\times 10^{-3}$ and 10^{-2} M_⊙ yr⁻¹. The comparison also highlights some limitations of the Hill5 method. We demonstrate that the width of optically thin spectral lines, which are usually interpreted as resulting from turbulent motions, are in fact dominated by unresolved, ordered infall motions within the beam. Our results suggest a complex collapse situation where there is a minimum in the infall velocity at $\sim 2 \times 10^{18}$ cm (0.7 pc) with the infall velocity increasing at both smaller and larger radii. The parsec-scale infall with an inverted velocity profile indicates that the accretion in this massive star-forming cloud should have intermediate scales, at which fragmentation or filament formation has to occur before material flows onto the cloud centre.

Key words: stars: formation – ISM: clouds – ISM: kinematics and dynamics – ISM: individual (SDC335.579-0.292/IRAS 16272-4837)

1 INTRODUCTION

Gravitational collapse is the basic step in star formation (e.g. Shu 1977; Elmegreen & Lada 1977; Vázquez-Semadeni et al. 2017) and the nature and evolution of this collapse are central in determining the masses of the stars, hence their destinies. When gas is infalling, differences in the excitation temperatures across the cloud can cause self-absorption features in optically thick molecular line profiles

with the emission to the blue side of the absorption being of a higher intensity than the red. Meanwhile, the optically thinner species peak in the self-absorption dip of the optically thicker lines (e.g. Snell & Loren 1977; Walker et al. 1986; Anglada et al. 1987).

Such characteristic molecular line profiles have been observed towards both low- and high-mass star-forming regions (e.g. Zhou et al. 1993; Myers et al. 1995; Wu & Evans 2003; Fuller et al. 2005; Wu et al. 2010). Infall properties such as the velocity profiles and radius of the infall region have been studied with various methods and have been further used to calculate crucial star-forming param-

* E-mail: dili@mail.tsinghua.edu.cn, gary.a.fuller@manchester.ac.uk

eters including mass accretion rates and accretion timescales (e.g. López-Sepulcre et al. 2010; Rygl et al. 2013; Calahan et al. 2018; Xu et al. 2023a). However, analyses of hydrodynamic simulations have shown that a prominent blue-asymmetric line profile may not be observable, even if there is infall (Smith et al. 2012).

Early infall studies mainly focused on low-mass nearby regions including starless cores with the exploration of different tracers (e.g. Zhou et al. 1993; Myers et al. 1995; Lee et al. 2001). In recent years, more observations have revealed global collapse appearing in massive star-forming regions (e.g. Wu & Evans 2003; Fuller et al. 2005; Wu et al. 2010; Peretto et al. 2013; Jackson et al. 2019; Yang et al. 2023; He et al. 2023; Jackson et al. 2026). Semi-analytic models such as the ‘two-layer’ model (Myers et al. 1996) and the ‘Hill’ model (De Vries & Myers 2005), use simplifying assumptions on the physical properties of a region to derive an analytic form for the blue asymmetric line profile and so provide an estimate of the infall velocity. These methods have been widely used to infer the infall velocities from molecular line observations of star-forming regions (e.g. Schneider et al. 2010; Zapata et al. 2013; Qin et al. 2016; Xie et al. 2021a). One-dimensional models including radiative transfer (RT) (e.g., RATRAN (Hogerheijde & van der Tak 2000)) have been applied to derive infall velocity by simulating infall profiles and comparing these with observations (e.g. Peretto et al. 2013; Olguin et al. 2021; Yang et al. 2023). To fully understand the collapse scenario of a cloud, RT modelling of the observations is needed.

Simulations on infall profiles have been carried out towards star-forming regions. Detailed modelling of a low-mass star-forming region B335 (Evans et al. 2015) shows the infall is consistent with a free-fall velocity profile ($\propto r^{-1/2}$ where r is the distance from the central source) and L483 is well modelled by a profile with $v_{\text{in}} \propto r^{-1}$ (Jacobsen et al. 2019). The three-dimensional line RT code, LIME (LIne Modeling Engine) (Brinch & Hogerheijde 2010) has been recently used to study ^{13}CO infall velocities varying within the infall region towards B335, from which the models could reproduce high infall velocities on larger scales and maintain low velocities close to the protostar simultaneously when infall velocities deviated from free-fall velocities (Bjerkeli et al. 2023). Studies of the density profiles in simulations of cores also suggest that the infall velocities may be larger at larger radii (Gómez et al. 2021), an ‘outside-in’ collapse (Elmegreen & Lada 1977). However, such modelling of infall velocity profiles for studying global collapse, especially simulations for observational molecular line profiles, towards massive star-forming regions are still lacking.

1.1 The massive-star-forming IRDC SDC335.579-0.292

One extensively studied massive star-forming region is the Infrared Dark Cloud (IRDC) SDC335.579-0.292 (hereafter SDC335, also known as IRAS 16292-2722). SDC335 (e.g. Peretto et al. 2013; Avison et al. 2021; Olguin et al. 2022; Xu et al. 2023b), located at a distance of 3.25 kpc, spans a diameter of 2.4 pc (Peretto et al. 2013). The total mass is calculated to be $5500 \pm 800 M_{\odot}$ with 3 young OB stars forming in the region (Peretto et al. 2013; Avison et al. 2015). Global collapse was identified in the $\text{HCO}^+ \text{J}=1-0$ observations with infall signatures seen over the extended region of the clump (Peretto et al. 2013). An overview of the region is shown in the upper panel of Figure 1.

To deduce the underlying velocity field that gives rise to a given line profile in a region like SDC335 is, however, a non-trivial task. Detailed RT simulations are needed to estimate infall velocities. Avison et al. (2021) showed that the outflow rates are consistent with

mass accretion rates in the inner circumstellar region comparable to the mass accretion rate in the surrounding clump. Previously RATRAN (Hogerheijde & van der Tak 2000) and the analytic ‘two-layer’ model (Myers et al. 1996) were used to analyse the peak HCO^+ spectrum of SDC335 and suggest that this cloud is collapsing at a speed of 0.7 km s^{-1} (Peretto et al. 2013). While simple to use and widely adopted to provide an estimate of infall velocities, parametric models like the ‘two-layer’ model (Myers et al. 1996) and the ‘Hill’ model (De Vries & Myers 2005) (see Sec. 3.1 for details) assume a uniform infall velocity. However, it is unclear whether this is the case in collapsing regions. In this work, we carry out a modelling study of the spectral maps of SDC335 to spatially resolve the infall properties.

As noted by Peretto et al. (2013), SDC335 shows a spatially extended distribution of blue asymmetric $\text{HCO}^+ \text{J}=1-0$ line profiles characteristic of infall. In Appendix A we describe the possible parameterisation of this asymmetry. One such parameterisation is P_r , the ratio of the intensity of the blue-shifted peak to that of the red-shifted peak. Figure 1 (lower panel) shows the spatial distribution of P_r across SDC335. The map shows that the spectroscopic signature of infall is seen over a significant portion of the clump. Note that at positions towards SDC335 (and in general) where the line profile is asymmetric (due to infall) but does not have clear double peak, the parameter P_r is poorly defined. Moreover, while providing a description of the line shape, P_r (and the other parameters described in Appendix A) do not on their own provide any estimate of the properties of the infall. To do this requires a model. The simplest and most widely used are models based in a simple layer approximation (Myers et al. 1996), with the most sophisticated of these being the ‘Hill’ model (De Vries & Myers 2005). For our analysis in this work we define the central position of the clump as the pixel close to the peak of the clump with the largest value of the parameter P_r . This pixel is at position $(l,b) = 335.5836^{\circ}, -0.2862^{\circ}$ and is indicated by the red cross in Figure 1.

We describe the observational data and the models in Section 2 and the methods we used to characterise the infall signatures and the quantitative comparison method to evaluate the results are described in Appendix A. The analyses from the semi-analytic model are described in Section 3. RT models used are described in Section 4, which also includes the results from RT models such as RATRAN (Hogerheijde & van der Tak 2000), RADMC-3D¹ (Dullemond et al. 2012), and LIME (Brinch & Hogerheijde 2010), as well as the comparisons among the RT models and the semi-analytic model. The robustness of the semi-analytic model is examined through comparisons with the inputs of the RT models across the cloud. The effects from underlying assumptions such as uniform infall velocities on the results of models are explored and compared with the observed data. We discuss the discrepancies among the models, the sensitivity and the accuracy of the analytic model, and the implications on massive star formation in Section 5. Section 6 summarises our results which quantitatively reproduce the observations of SDC335 with our best-fit models and the obtained infall velocity and mass infall rate.

2 OBSERVATIONAL DATA

We use the observations of $\text{HCO}^+ \text{J}=1-0$ at 89.188518 GHz (Pickett et al. 1998) and $\text{H}^{13}\text{CO}^+ \text{J}=1-0$ at 86.7542884 GHz together

¹ <http://www.ita.uni-heidelberg.de/~dullemond/software/radmc-3d>

with $\text{N}_2\text{H}^+ J=1-0$ at 93.173772 GHz from the MALT90 survey undertaken with the Mopra 22 m single-dish telescope² (Foster et al. 2011, 2013; Jackson et al. 2013). The systemic velocity of the cloud, -46.5 km s^{-1} , was derived from the optically thin lines $\text{H}^{13}\text{CO}^+ J=1-0$ and $\text{N}_2\text{H}^+ J=1-0$. At this frequency, the angular resolution of the Mopra telescope is $\sim 37''$ (Ladd et al. 2005), corresponding to 0.43 pc at the distance of SDC335. The $\text{HCO}^+ J=1-0$ line has the blue asymmetric profile (Figure 2) characteristic of infall over a ~ 3 pc-sized region of the clump (Peretto et al. 2013). The velocity resolution is 0.1 km s^{-1} with the rms $\sim 0.2 \text{ K}$ on T_{mb} scale. We smoothed the data by 2.5 channels (giving a final spectral resolution of 0.25 km s^{-1}), which reduced the rms to 0.013 K as this allows better characterisation of the main features of the blue asymmetric profiles. In the following analysis, the models are all rebinned to match this resolution.

The N_2H^+ observations are only used to provide an estimate of the dense gas velocity for comparison with the HCO^+ spectra at some positions in the clump. The velocity at these positions is determined from a fit to the hyperfine components using the pyspeckit fitting routine adopting a frequency of 93.1737637 GHz for the $F_1 = 2, F = 3$ to $F_1 = 1, F = 2$ hyperfine component (Pagani et al. 2009).

To account for the telescope efficiency and the coupling of the source to the telescope beam (the beam filling factor), when comparing the models with the observations, the peak intensities of the modelled spectral lines were scaled by a factor η to match the peak intensity of the observed line. Ladd et al. (2005) gives efficiencies for the Mopra telescope of $\eta_{\text{mb}} = 0.49$ for compact sources and 0.65 for more extended sources such as the case for SDC335. The scaling factor applied to the models, η , was always < 0.7 , which is consistent with the measured telescope efficiency within the uncertainties. So the emission from models that would require an efficiency significantly larger than ~ 0.7 would be too weak to match the observations. On the other hand, values of $\eta < 0.7$, would correspond to the source not completely filling in the telescope beam. In the modelling discussed below the values of η required to match the models to the observations were consistent with the range $0.49 < \eta < 0.7$, except for the RATRAN model, which required the slightly larger value of 0.8.

3 INFALL PROPERTIES: SEMI-ANALYTIC MODEL

To probe the infall properties in SDC335, we first use a one-dimensional semi-analytic model, the ‘Hill’ model. The ‘Hill’ model is considered to be an upgraded model of ‘two-layer’ model (Myers et al. 1996), which tends to underestimate the infall velocities (De Vries & Myers 2005). The ‘Hill’ model assumes a hill-shape excitation temperature distribution of gas across the cloud, as compared with the earlier ‘two-layer’ model which adopted two excitation temperature layers in the cloud. Hill5 is a model with five free parameters, which are optical depth τ , infall velocity v_{in} , systematic velocity v_{lsr} , velocity dispersion σ , and peak excitation temperature T_p . The Hill5 has been considered the most robust model among the Hill models with different sets of free parameters (De Vries & Myers 2005). The Hill5 model has been applied to calculate infall velocities in other massive star-forming regions including other IRDCs, as well as low mass star-forming regions (e.g. Williams et al. 2006; Contreras et al. 2018; Calahan et al. 2018).

² <https://www.narrabri.atnf.csiro.au/mopra/>

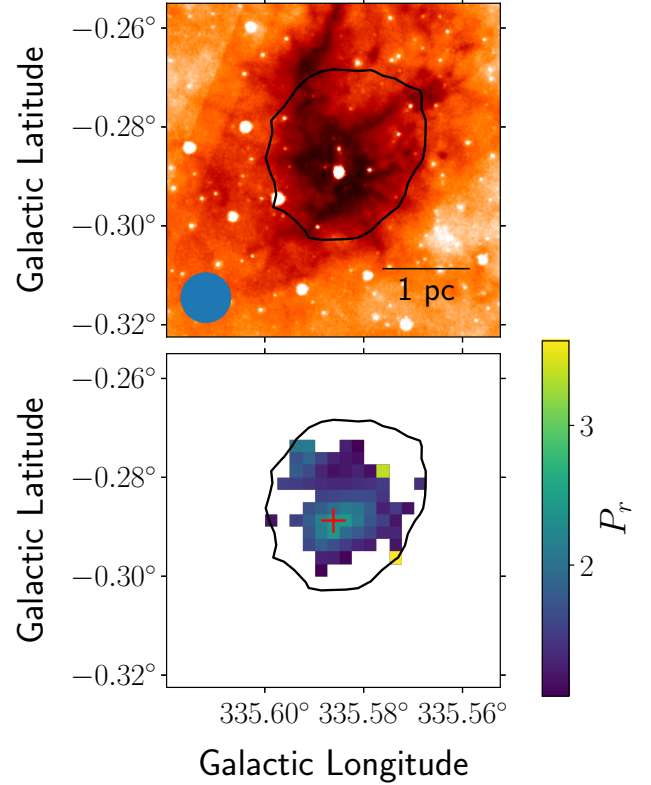


Figure 1. *Upper:* Spitzer GLIMPSE (Churchwell et al. 2009) $8 \mu\text{m}$ image of SDC335 showing the absorption tracing the densest regions of the clump. The beam of the $\text{HCO}^+ J=1-0$ observations is shown in the lower left and a 1 pc scale bar is shown in the lower right. *Lower:* The spatial distribution of the P_r , the intensity ratio of the blue-shifted peak to the red-shifted peak (Sec. A). The parameter P_r is evaluated for the region where the integrated intensity (the 0th-order moment emission map) is $> 20\%$ of the peak integrated intensity in the line (as indicated by the contour) on both panels. The red cross marks the pixel closest to the centre of the clump with the largest value of P_r .

3.1 Hill5 Model Description

In the ‘Hill’ model, the brightness temperature of the molecular line above the background, $\Delta T_B(v)$, is given by

$$\Delta T_B(v) = (J(T_p) - J(T_0)) \left[\frac{(1 - e^{-\tau_f(v)})}{\tau_f(v)} - e^{-\tau_f(v)} \frac{(1 - e^{-\tau_r(v)})}{\tau_r(v)} \right] + (J(T_0) - J(T_b)) \left[1 - e^{-\tau_r(v) - \tau_f(v)} \right], \quad (1)$$

where T_B is the brightness temperature defined as $T_B = (c^2/2\nu^2k)I_\nu$, and I_ν is the specific intensity. $J(T)$ refers to the Planck average energy or the Planck-corrected brightness temperature where $J(T) = (h\nu/k) \left[\exp(h\nu/kT) - 1 \right]^{-1}$. The excitation temperature at the near and far edges of the source, along the line of sight, is T_0 . The optical depth of the foreground material where the excitation temperature is rising along the line of sight is τ_f , while τ_r is the optical depth along the line of sight in the region beyond the peak excitation temperature. A uniform velocity dispersion σ is assumed for the entire cloud. The optical depths at velocity v for the foreground and background (rear) layers are given by

$$\tau_f(v) = \tau \exp \left[- (v - v_{\text{lsr}} - v_{\text{in,Hill5}})^2 / 2\sigma^2 \right], \quad (2)$$

Table 1. Best-fitting Hill5 parameters for the central pixel.

τ	v_{lsr} (km s ⁻¹)	$v_{in,Hill5}$ (km s ⁻¹)	σ_v (km s ⁻¹)	T_p (K)
2.77 ± 0.09	-46.38 ± 0.02	-1.19 ± 0.04	1.05 ± 0.02	10.71 ± 0.20

$$\tau_r(v) = \tau \exp \left[- (v - v_{lsr} + v_{in,Hill5})^2 / 2\sigma^2 \right]. \quad (3)$$

A Python fitting code using Python package LMFIT³ was developed with the above equations, which requires an initial guess as an input for the five free parameters, τ , infall velocity $v_{in,Hill5}$ ⁴, systematic velocity v_{lsr} , velocity dispersion σ , and peak excitation temperature T_p ⁵. We also used the Hill5 fitter in the PySpecKit (Ginsburg & Mirocha 2011) package⁶ and found to be in excellent agreement with our own independent implementation of the routine which was developed to confirm the form of the equations.

3.2 The Central Pixel

The best-fit results of infall parameters for the central pixel on the observed HCO⁺ J=1–0 map from Hill5 are listed in Table 1 and the fitted spectra are shown in Figure 2. The uncertainties are estimated from Markov Chain Monte Carlo (MCMC) sampling used with 5×10^5 samples. Figure 3 shows the distribution of the fit parameters with their mean and effective 1- σ uncertainties (as given by the 16th and 84th percentiles of the distributions). The marginalised distributions show that there is some correlation between the fitted v_{lsr} and the optical depth (τ). A correlation is also seen between the velocity dispersion (σ) and infall velocity ($v_{in,Hill5}$), although both are well constrained with formal uncertainties of ± 0.02 km s⁻¹ and ± 0.04 km s⁻¹, respectively.

3.3 The Spatial Distribution of the Infall Velocity

The map of the infall velocities estimated by Hill5 for all the spectra in the HCO⁺ cube is shown in Figure 4. The map shows that moving outward from the central pixel, the fitted infall velocity initially decreases. Over most of the map, the infall velocity reaches close to zero around the contour corresponding to the line reaching 20% of its peak flux. However, towards the northeast, the Hill5 fit gives consistently larger values for $v_{in,Hill5}$ than the $[-0.75, -0.5]$ km s⁻¹ in the minimum around the central pixel, but the values have significant scatter, pixel to pixel.

Figure 5 shows the infall velocity variation as a function of the radius from the central pixel from the map in Figure 4. The red points show the infall velocity averaged over radial bins 10'' wide. Although there are significant uncertainties, both the values for individual pixels and the binned values show the derived infall velocity decreases in magnitude from the central pixel out to a radius of about 40'' ($\sim 2 \times 10^{18}$ cm or 0.65 pc). Beyond this, there is

³ <https://lmfit.github.io/lmfit-py/>

⁴ We adopt the convention that the infall velocity, v_{in} , is negative for motion towards the centre of the region. In comparisons of the speed of the infall we will use the magnitude of v_{in} , such that faster infall will correspond to more negative values, and this is referred to as larger values throughout the text.

⁵ Equation 1 is typeset incorrectly in the Astrophysical Journal in (De Vries & Myers (2005)). The correct version can be found in the arXiv version of the paper.

⁶ https://pyspeckit.readthedocs.io/en/latest/hill5infall_model.html#module-pyspeckit.spectrum.models.hill5infall

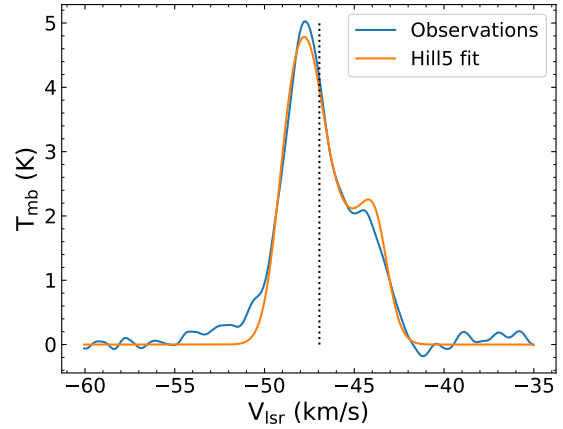


Figure 2. Spectrum towards the central pixel and the Hill5 fit to it. The fitted parameters are listed in Table 1. The dotted vertical line indicates the central velocity of N₂H⁺ J=1–0, -46.9 ± 0.1 km s⁻¹. This velocity is somewhat different from the velocity derived from the Hill5 fit which refers to the central velocity of the currently infalling, lower density gas.

Table 2. Sizes of the annular regions used to construct averaged spectra.

Aperture	Inner radius (arcsec)	Outer radius (arcsec)	Aperture central radius (arcsec)	central radius (10 ¹⁸ cm)
A1	18.6	37.2	28	1.4
A2	37.2	55.8	47	2.3
A3	55.8	73.8	65	3.2

a significant scatter (as seen in Figure 4), though the binned values suggest a relatively uniform value of v_{in} of ~ -1 km s⁻¹.

Hill5 has been widely applied to infer infall velocities and sometimes on the averaged spectra of a certain radius (e.g. Contreras et al. 2018; Xu et al. 2023a; Yang et al. 2023). For SDC335, we show the spectra and the fitted spectra in the central region averaged over annular regions in Figure 6, of which the details are listed in Table 2. The values for the infall velocity for these annularly averaged spectra are in excellent agreement with the averaged fit values in the comparable range of radius. They show the infall velocity increasing from -1.19 ± 0.02 km s⁻¹ at the central pixel to -0.58 ± 0.01 km s⁻¹ at a radius of 47'' (2.2×10^{18} cm or 0.71 pc). Hill5 therefore seems to consistently indicate a decrease in the infall velocity with increasing distance from the centre of the source to out to radii $\sim 50''$ ($\sim 2.5 \times 10^{18}$ cm or 0.81 pc).

To explore the line profiles more distant from the centre, the data have been averaged over the five beam-sized regions shown in Figure 4. Four of these beam-sized regions were selected to sample the outer region of the clump where Hill5 found large infall velocities in the pixel-by-pixel fitting. The fifth region was selected as a test in a region where the pixel-by-pixel Hill5 fits found no infall. The spectra and their Hill5 fits are shown in Figure 7. This figure shows that the four regions (labelled A to D) all show HCO⁺ spectra which are blue asymmetric (asymmetric with brighter blue peaks than red peaks) with respect to the velocity of dense gas in the same region (as traced by N₂H⁺). The Hill5 fits indicate infall velocities in the range -0.8 to -1.1 km s⁻¹, consistent with the average values from fits to the individual spectra. At these larger distances, $> 50''$, Hill5 suggests an *increased magnitude* for the infall velocity towards the outer region compared to the region closest to the central source, over at least part of the clump. Region E in Figure 4 covers an

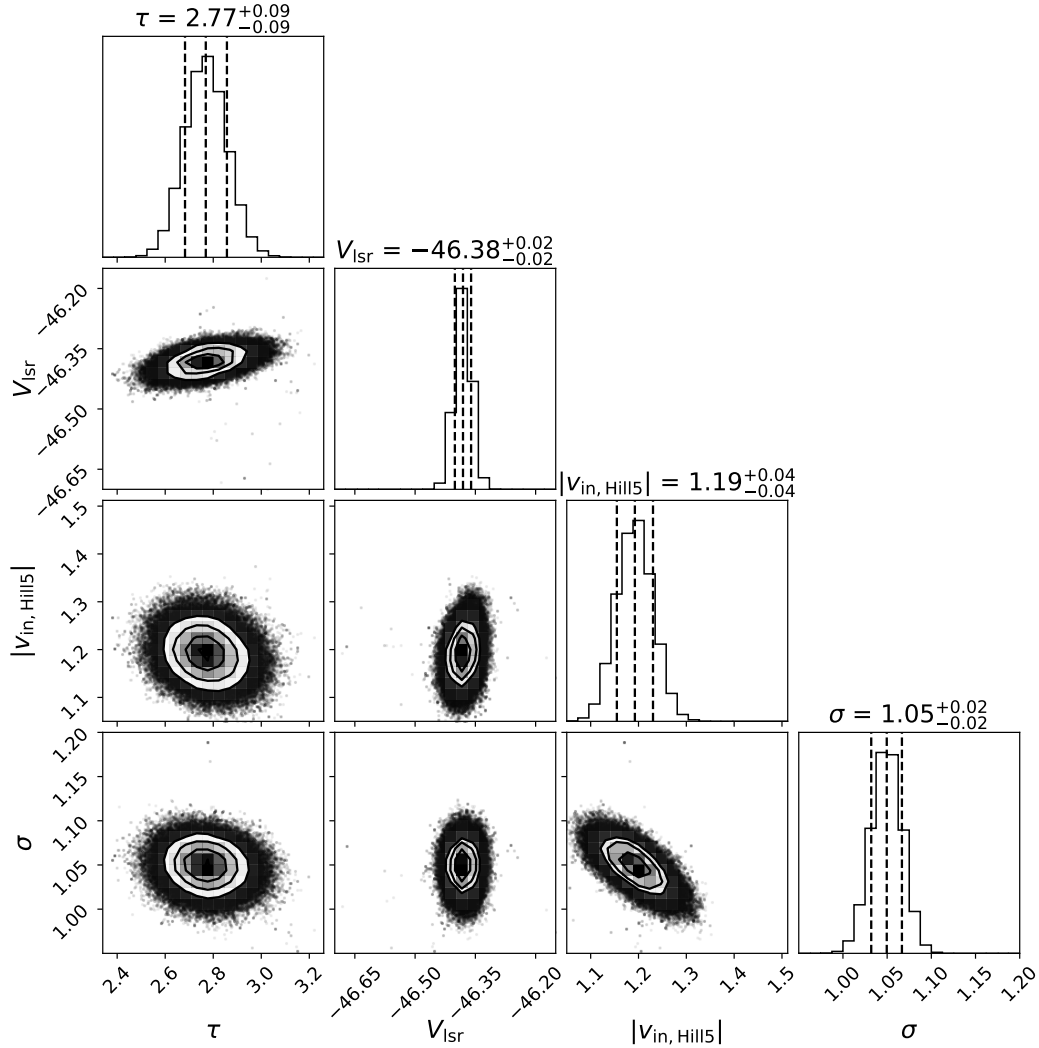


Figure 3. Corner plot showing the distribution of fit variables for 50 000 Markov Chain Monte Carlo (MCMC) evaluations of the Hill5 fit to the central $\text{HCO}^+ J=1-0$ spectrum. The marginal distributions for each variable shown at the top of each column are labelled by the median value and their $1-\sigma$ equivalent uncertainties. The lower panels show the distribution of the fit values in the parameter planes. The distribution of points in high density parts is shown in contours and as points in the lower density regions. The peak excitation temperature was included as part of fit, but is not shown here.

area where Hill5 could not identify the presence of infall and the aperture averaged spectrum of this region (Figure 7), although not fully symmetric, does not show a blue asymmetry and the peak velocity agrees closely with that of N_2H^+ and so shows no evidence of infall. This is consistent with the larger Pr values found in the same region in Figure 1.

4 INFALL PROPERTIES: RT MODELS

To explore how the values derived by Hill5 map on to the actual infall properties in more complex situations, we have modelled clumps with a wider range of infall properties such as infall velocities and infall radii and compared the infall values estimated by Hill5 with the true infall properties. For this we adopted three RT models, namely LIME, RADMC-3D, and RATRAN. LIME is a 3-D RT non-LTE (Local Thermodynamic Equilibrium) accelerated Lambda Iteration code with uses unstructured 3-D Delaunay grids for photon transport (Brinch & Hogerheijde 2010). RADMC-3D is a 3-D RT package

developed by Dullemond et al. (2012) for dust and molecular lines. The line transfer can be performed assuming LTE or the LVG (Large Velocity Gradient) approximation. RATRAN is a 1-D Cartesian grid Monte Carlo code which includes elements of accelerated Lambda iteration (Hogerheijde & van der Tak 2000). The molecule data files are from the Leiden database LAMDA⁷ (Schöier et al. 2005).

Initially, the comparison with the observations was focused on comparing the central pixel in the model with the observed spectrum at the centre of the clump. Before this comparison, the models were convolved with a $37''$ FWHM (full width at half maximum) Gaussian to simulate the Mopra beam at the frequency of $\text{HCO}^+ J=1-0$ (Ladd et al. 2005) and regridded to the same spectral channels as the observations.

⁷ <https://home.strw.leidenuniv.nl/~moldata/>

Table 3. Best fit parameters to the central pixel from the RT models.

Label	p	Model	v_c (km s ⁻¹)	Δv_b (km s ⁻¹)	σ_v (km s ⁻¹)	Peak Intensity (K)	η	R
LIME								
1.5								
$M_{LIME,0}$		$f = 1/2$	-1.40	1.50	1.06	7.9	0.64	1.11
$M_{LIME,1}$		$f = 1$	-1.10	1.60	1.13	7.5	0.67	1.09
$M_{LIME,2}$		$f = 1, T=20$ K	-1.40	1.40	1.06	8.0	0.63	1.06
$M_{LIME,3}$		$f = 3/2$	-1.00	1.60	1.13	7.7	0.65	1.08
2.0								
$M_{LIME,4}$		$f = 1/3$	-1.40	1.50	1.06	8.9	0.57	1.13
$M_{LIME,5}$		$f = 1/2$	-1.50	1.50	1.06	9.3	0.54	1.13
$M_{LIME,6}$		$f = 1$	-1.10	1.60	1.13	8.7	0.57	1.11
$M_{LIME,7}$		$f = 1, T=20$ K	-1.30	1.50	1.06	8.8	0.57	1.05
$M_{LIME,8}$		$f = 1, 2R^*$	-1.30	1.60	1.13	9.2	0.55	1.10
$M_{LIME,9}$		$f = 3/2$	-0.80	1.70	1.20	8.0	0.63	1.12
$M_{LIME,10}$		$f = 3$	-0.60	1.70	1.20	8.1	0.62	1.11
$M_{LIME,11}$		$v_{in} \propto r^{-0.5}$	-1.50	1.50	1.06	9.0	0.56	1.13
RADMC-3D								
$M_{RADMC3D}$	1.5	$f = 1, T=20$ K	-1.60	1.83	1.30	8.5	0.58	1.09
RATLAN								
M_{RATLAN}	1.5	$f = 1, T=20$ K	-0.90	1.60	1.13	6.3	0.78	1.16

Note: All the models have a temperature profile as described in the text, except those noted as T=20 K which have a uniform temperature of 20 K. *Model with outer radius twice that of the other models. The uncertainties on both v_c and Δv_b are estimated to be ~ 0.1 km s⁻¹, the sampling used in generating the grids of simulations. The peak intensities listed are not corrected for the telescope efficiency. However, an efficiency factor has been applied when model spectra are plotted for comparison with the observations. Note that $\sigma_v = \Delta v_b / \sqrt{2}$.

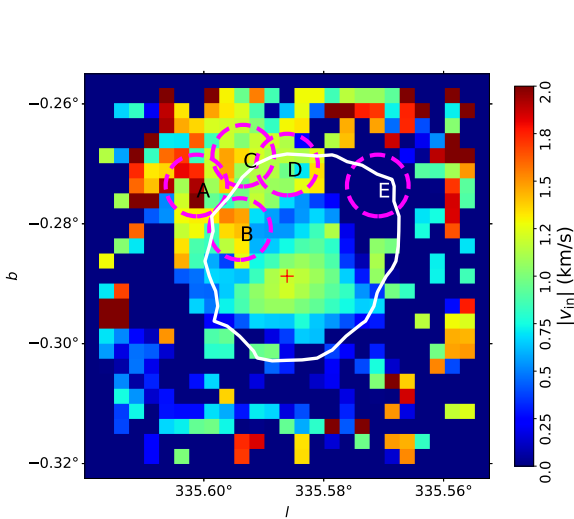


Figure 4. The spatial distribution of the magnitude of the infall velocity ($|v_{in}|$) derived from Hill5. The red cross marks the central pixel. The magenta circles show the regions over which the spectra shown in Figure 7 are extracted. The white contour labels of the 20% of the peak integrated intensity.

4.1 Physical Parameters for Models

To model the line profiles, we need to define a physical description of the properties of SDC335. Specifically these are the density profile,

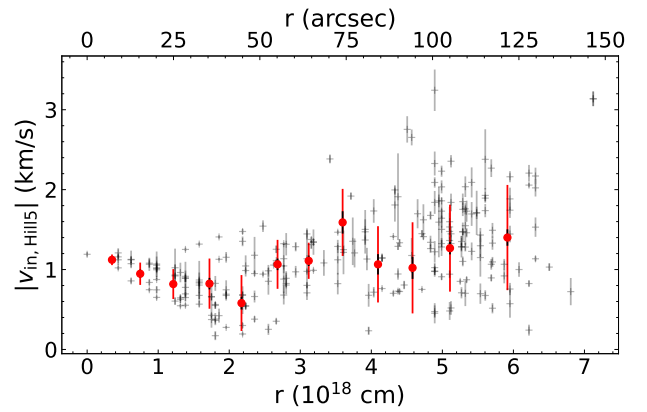


Figure 5. Hill5-fitted infall velocity, $v_{in,Hill5}$, as a function of radius from the central pixel. The grey points show the values for the individual pixels in the map with the uncertainties from their fits which are typically $\sim 0.1 - 0.2$ km s⁻¹. The red points show these binned in bins of $10''$. The red points are plotted at the average radius of the points averaged in that bin. The red error bars show the dispersion of values used to calculate the average.

the temperature profile, turbulence, the abundance of HCO⁺, as well as the infall velocity. Since the SDC335 clump appears round with little evidence of significant elongation at the resolution of the observations used here, we model SDC335 as a sphere of radius 1.2 pc with the physical parameters dependent only on the radius, r , within the clump.

Modelling of high mass clumps has shown that their density distributions are well fitted with density profiles of the form $\rho(r) \propto$

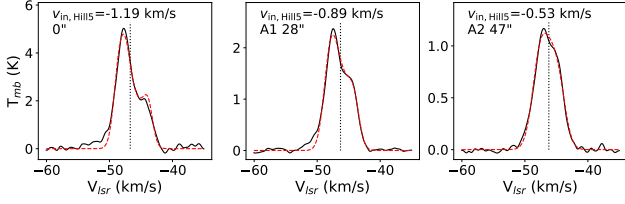


Figure 6. Annular average spectra and Hill5 fits. The panels show the HCO⁺ spectra at the central pixel (left) and averaged over annuli of width 18.6'' with radii of 28'' (middle) and 47'' (right) respectively (as described in Table 2). The black curve shows the data and the vertical markers show the velocity derived from the N₂H⁺ spectra averaged over the same regions. The dashed red curve shows the Hill5 fits to the spectra with the fitted infall velocity indicated in the respective panel.

r^{-p} typically with $1 \leq p \leq 2$ (e.g. Beuther et al. 2002; Williams et al. 2005; Palau et al. 2014; Wyrowski et al. 2016). The measurements of SDC335 show that it is relatively symmetric, highly centrally condensed, with Peretto et al. (2013) showing that SDC335 has a mass distribution consistent with $p \sim 2$. We, therefore, adopted $p = 2$ but also explored some models with $p = 1.5$ for comparison with Peretto et al. (2013) and to explore the sensitivity of our results to the assumed density profile. The normalisation of the density profile was constrained to match the observed total mass within 1.2 pc of 5500 M_⊙ (Peretto et al. 2013).

To determine the temperature structure for our spectral line models, we used RADMC-3D, which can self-consistently calculate the temperature profile, to derive the temperature of our adopted density profiles ($p = 2$ and $p = 1.5$) assuming a central heating source. However, in the outer regions of the clump, the temperature was fixed at a minimum of 20 K, consistent with the uniform temperature adopted by Peretto et al. (2013) and the measured temperatures of the outer regions of IRDCs (e.g. Ragan et al. 2006; Xie et al. 2021b). The outflows from the embedded sources in SDC335 indicate a mass accretion rate onto the protostars of 1.4×10^{-3} M_⊙ yr⁻¹ (Avison et al. 2021). At this high accretion rate Hosokawa & Omukai (2009) and Hosokawa et al. (2010) show that the central protostar is bloated with a lower surface temperature than would be expected for its luminosity. Therefore, in the RADMC-3D model, we assumed the central source had a luminosity 2×10^4 L_⊙ and a surface temperature of 3000 K. The resulting adopted temperature profiles for a $p = 2$ and a $p = 1.5$ density profile are shown in Figure 8. In addition, some models were also run with a uniform temperature of 20 K to allow both a more direct comparison with Peretto et al. (2013) and also to assess the impact of the temperature profile on the line profiles.

We adopt a uniform HCO⁺ abundance of 7×10^{-10} , consistent with the value used by Peretto et al. (2013). As discussed by Peretto et al. (2013), at the galactocentric radius of SDC335 the expected abundance ratio ¹²C/¹³C (and so the abundance ratio H¹²CO⁺/H¹³CO⁺) is 30, but Peretto et al. (2013) measured a value of 20. We use this observed ratio in modelling the H¹³CO⁺ lines. Also an abundance ratio of 30 results in lines that are too weak to match the observations.

We explore models where the infall velocity, $v_{in}(r)$, is a function of radius, r , within the clump. The form of $v_{in}(r)$ adopted is

$$v_{in}(r) = \begin{cases} v_c & r \leq r_c \\ v_c + v_c(f-1) \frac{r-r_c}{R_0-r_c} & r_c < r \leq R_0 \end{cases} \quad (4)$$

where r is the distance from the clump centre, r_c is the radius of the central region which has a uniform infall velocity of v_c , R_0 is the

maximum radius (1.2 pc), and the factor f which describes the infall velocity at R_0 as a multiple of v_c . A value of $f = 1$ corresponds to a uniform infall velocity across the region. For all the models $r_c = 0.3$ pc which corresponds to the beam size of the HCO⁺ observations. The range of factors f by which v_{in} increases and decreases with radius is selected based on an initial set of comparisons which suggested that values $1/3 \leq f \leq 3$ provided reasonable fits to the spatial distribution of the infall line profiles. In addition, a model with $p = 2$ and where the infall velocity is described by

$$v_{in}(r) = \begin{cases} v_c & r \leq r_c \\ v_c \left(\frac{r_c}{r}\right)^{1/2} & r_c < r \leq R_0, \end{cases} \quad (5)$$

to mimic a gravitational free-fall collapse is also investigated.

4.2 The Central Pixel

All the best fit models for the central pixel are summarised in Table 3. To assess the discrepancy between our modelled line profiles and the data we use the statistic, R ,

$$R = \frac{1}{N_c} \sum_i A_i \quad (6)$$

where

$$A_i = \begin{cases} d_i/m_i & \text{if } d_i \geq m_i \\ m_i/d_i & \text{if } d_i < m_i, \end{cases} \quad (8)$$

d_i and m_i are the intensity of the observed spectrum and the model spectrum in pixel i respectively, so the statistic measures the ratio to the model to the data. The statistic is calculated over the velocity range $w_{1/2}$ (Appendix A) and N_c is the number of spectral channels in this velocity range. The R statistic is more suitable for comparing models and observations than the parameters often used to characterise observed line profiles (Appendix A) since R is well defined even if the line profiles do not have a clear double peak structure (Sec. 1.1). The statistic R is also more suitable for fitting the overall line profile than the usual χ^2 statistic which can result in fits which are dominated by differences between the model and observations in strong features at the expense of fitting weaker features.

To find the best fit infall velocity v_{in} and velocity dispersion, σ_v , we ran grids of models with different infall velocities and velocity dispersions. LIME describes the velocity width of the gas in terms of the Doppler- b parameter, $\Delta v_b = \sqrt{2}\sigma_v$, where σ_v is the velocity dispersion. The grids of LIME models were sampled at 0.1 km s⁻¹ in v_{in} and 0.1 km s⁻¹ in Δv_b . An example grid of LIME models is shown in Figure 9, corresponding to model $M_{LIME,7}$ in Table 3 ($p = 2.0$, $f = 1$, and a constant temperature $T = 20$ K). Figure 10 presents contours of the R parameter on the v_c - σ_v plane.⁸

For direct comparison with Peretto et al. (2013), we also explored models with $p = 1.5$ and a uniform temperature of 20 K (see $M_{LIME,2}$ in Table 3). With these parameters, the best fit has an infall velocity of -1.3 km s⁻¹ and Doppler width of 1.5 km s⁻¹ (corresponding to a dispersion of 1.1 km s⁻¹), the same as for the $p = 2$ model ($M_{LIME,7}$). Peretto et al. (2013) found a similar velocity dispersion of 1.0 km s⁻¹, but a smaller in magnitude infall velocity of 0.7 km s⁻¹. However, it should be noted that they were also fitting a different dataset taken with the Mopra telescope.

⁸ The v_c - σ_v planes for the other $p = 2$ LIME models are shown in Figure B1. For this model, we find that the best fit for the central pixel is obtained with $v_{in} = -1.3$ km s⁻¹ and $\sigma_v = 1.06$ km s⁻¹ ($\Delta v_b = 1.50$ km s⁻¹). Similar v_c - σ_v planes of $p = 2$ models are shown in Figure B1.

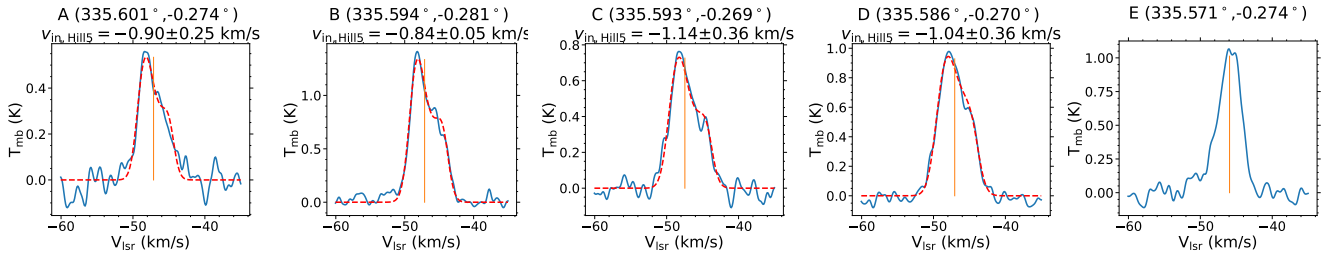


Figure 7. Spectra averaged over the circular regions shown in Figure 4. The central position (and label) of each spectrum is given above each panel. The data are shown in black and in the first four spectra the Hill5 fit is shown as the red dashed curve. For these positions the best fit infall velocity is shown in the title above the panel. Hill5 could not fit the spectrum at position E due to the lack of significant asymmetry in the line profile. The vertical line in each panel indicates the central velocity determined from a fit to the hyperfine structure of the N_2H^+ emission averaged over the same region as the HCO^+ .

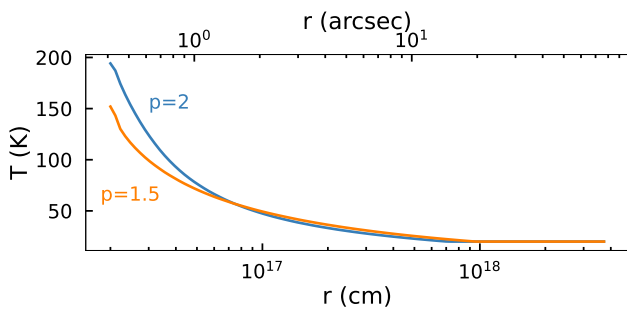


Figure 8. Temperature profiles determined by RADMC-3D for a central source of temperature 3000 K and a total luminosity of $2 \times 10^4 L_\odot$. The curves show the profiles for density profiles with $p = 1.5$ and $p = 2$ as labelled. The minimum temperature for both profiles was fixed at 20 K.

In addition, Peretto et al. (2013) used RATRAN, rather than LIME (Sec. 4.2.1).

Comparing uniform infall velocity ($f = 1$) models with a temperature profile ($M_{\text{LIME},1}$) with those with 20 K throughout (all with $p = 1.5$) ($M_{\text{LIME},2}$), shows that the presence of a temperature gradient results in an infall velocity 0.2 km s^{-1} smaller in magnitude and a velocity dispersion 0.1 km s^{-1} larger (Table 3). However, we do not consider these significant differences given the uncertainties in the fitting process and the underlying assumptions, and so our results suggest that density profiles have a negligible impact on the profiles.

A single model with twice the outer radius of the other models was also run to test for any influence of the size on the inferred infall properties. The best fit values from this model ($M_{\text{LIME},8}$) are very similar to the models with the smaller maximum radius, although the line peak temperature is higher.

Figure 11 compares the best fit models from grids of models with $p = 1.5$ ($M_{\text{LIME},1}$) and $p = 2$ ($M_{\text{LIME},6}$) density profiles (and matching temperature gradients). The upper panel of Figure 11 shows the HCO^+ while the lower panel shows H^{13}CO^+ . The two different density profile models have the same best fit values for the infall velocity and velocity dispersion, however, the lines they produce have different line peak intensities. The peak intensity of the HCO^+ line from the $p = 1.5$ model ($M_{\text{LIME},1}$) is 7.5 K while it is 8.7 K for the $p = 2$ model ($M_{\text{LIME},6}$). This is not apparent from the figure as the models are plotted adopting an efficiency factor to scale the model to the observed line peak intensity. Similarly for the H^{13}CO^+ where the $p = 1.5$ model ($M_{\text{LIME},1}$) predicts a weaker line peak temperature (1.2 K), than the $p = 2$ model ($M_{\text{LIME},6}$) with a peak temperature of 1.9 K.

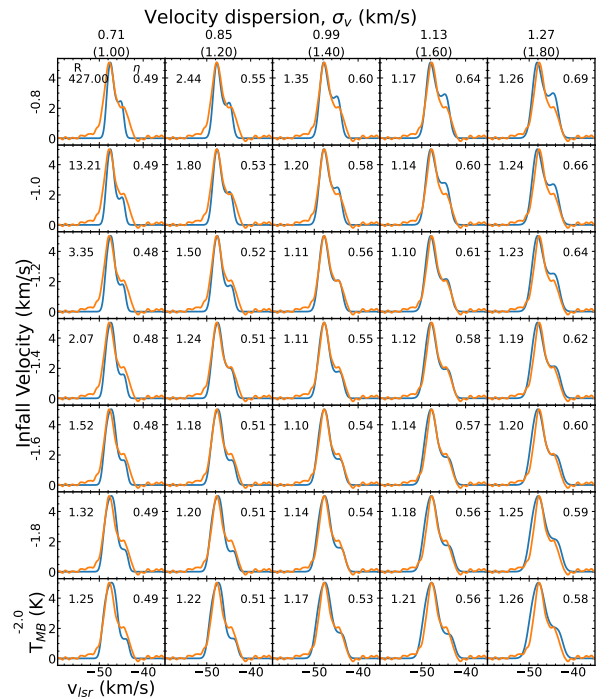


Figure 9. Comparison of a grid of LIME models with the emission at the central pixel. The models have a uniform infall velocity ($f = 1$, so $v_{\text{in}} = v_c$) in the clump with a $p = 2$ density profile and a uniform gas temperature of 20 K. In each sub-panel, the orange curve shows the observed spectrum at the central pixel and the blue curve shows the model of the indicated velocity dispersion and v_{in} . The value in the upper right of each sub-panel shows the scaling factor applied to the models (η) to match the peak of the observed line. The other value in each sub-panel shows the R statistic for the fit. For ease of display, the figure only shows a sub-sampled grid of the models, stepping by 0.2 km s^{-1} in both infall velocity and Δv_b whereas the complete grid of models is sampled at 0.1 km s^{-1} in both parameters.

Figure 12 shows the observations compared with the best fit models for five models with a range of values for f from $1/3$ to 3 while $p = 2$, i.e., $M_{\text{LIME},4}$, $M_{\text{LIME},5}$, $M_{\text{LIME},6}$, $M_{\text{LIME},9}$, and $M_{\text{LIME},10}$. Figures 11 and 12 show that all these models can reproduce the emission at the central pixel both for the HCO^+ and H^{13}CO^+ to a similar level, with the best fit models having R values between 1.08 (for the $M_{\text{LIME},3}$ model) and 1.13 (for several models). Figure 13 shows the adopted radial infall velocity profiles, where the parameter f controls whether the infall velocity decreases ($f < 1$), remains constant ($f = 1$), or increases ($f > 1$) with radius while

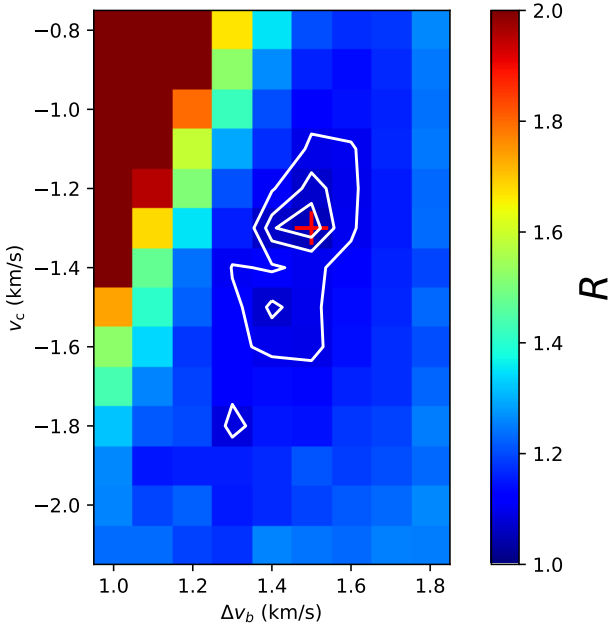


Figure 10. The $v_c - \Delta v_b$ plane for the grid of $f = 1$ models shown in Figure 9. The axes show the full range of $v_{in}(=v_c$ for these $f = 1$ models) and Δv_b explored. Both values were sampled every 0.1 km s^{-1} . The red cross marks the best fit model ($M_{LIME,7}$) which has $v_{in} = -1.3 \text{ km s}^{-1}$, $\Delta v_b = 1.50 \text{ km s}^{-1}$ ($\sigma_v = 1.06 \text{ km s}^{-1}$) and $R = 1.05$. The lowest contour shown has $R = 1.10$.

matching the same velocity at the central-pixel radius. As Figures 11, 13, and Table 3 show the choice of the structure of the infall velocity has a significant impact on the derived best fit v_{in} at the radius of the central pixel, v_c . Models with larger infall velocities in the outer regions of the clump require smaller infall velocities in the central region. Looking at the $p = 2$ models in Table 3, the inferred v_c increases in magnitude from 0.8 km s^{-1} for $f = 3$ ($M_{LIME,10}$) to 1.4 km s^{-1} for $f = 1/3$ ($M_{LIME,4}$). Fitting with a uniform infall velocity throughout the clump ($f = 1$, $M_{LIME,6}$) implies a central v_c of -1.1 km s^{-1} intermediate between the case where the infall velocity increases with radius and that where it decreases.

4.2.1 Comparison of Modelling Codes

To investigate the impact of using different RT to model the infall, in addition to LIME we used RATRAN and RADMC-3D to find the best fit parameters for models with uniform infall velocity, $p = 1.5$ and uniform temperatures of 20 K (using a grid-search method). The results for these models are also shown in Table 3 and these can be directly compared to the $p = 1.5$, $f = 1$ (20 K) models in the table. A comparison of the best fit results are presented in Figure 14. For comparison, the result of applying Hill5 to the central pixel is also shown in Figure 14 and Table 1.

The best fit results from the models are surprisingly different though all of them can fit the data reasonably well and to similar degrees of accuracy. The infall velocities from the three RT models, RATRAN, LIME, and RADMC-3D, span a range of a factor of 2, from -0.8 km s^{-1} (RATRAN) to -1.6 km s^{-1} (RADMC-3D). The spread in the inferred velocity dispersion, 0.3 km s^{-1} , is smaller but still significant while there is also a more than 1 K difference in the predicted line peak intensity. In each case, RADMC-3D produces the highest line intensity which may be related to the fact that the radiative transfer for the line emission in RADMC-3D is evaluated

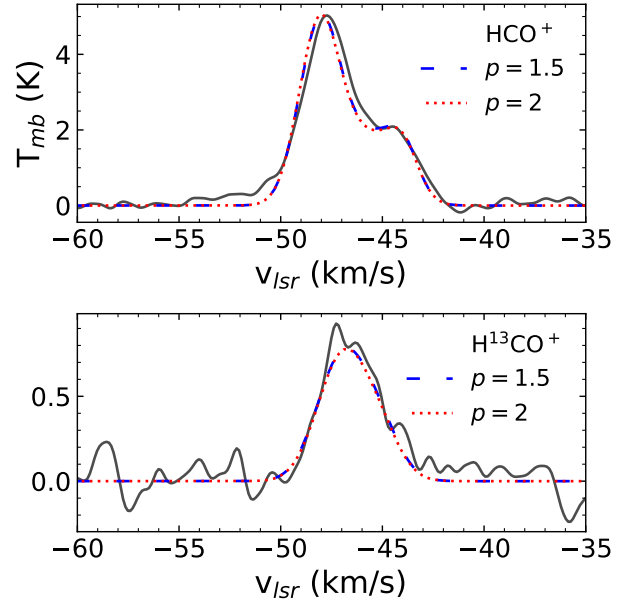


Figure 11. The central pixel profiles from two different density profiles in LIME models compared to the observational data. The models used temperature profiles with a minimum temperature of 20 K. *Left:* $\text{HCO}^+ J=1-0$ and *Right:* $\text{H}^{13}\text{CO}^+ J=1-0$. In each panel, the grey continuous line shows the observed emission at the central pixel. The red and blue broken curves show the best fit models for the density profiles with $p = 1.5$ and $p = 2$ with uniform infall velocities ($f = 1$). For both models, the infall velocity is -1.1 km s^{-1} and $\Delta v_b = 1.6 \text{ km s}^{-1}$.

in the large velocity gradient approximation which results in a lower optical depth at a given velocity and so requires a large velocity to match the observed line width while also tracing higher excitation temperature regions of the model. The comparison of the line shape at the central pixel of these models ($M_{LIME,7}$, $M_{RADMC3D}$, and M_{RATRAN}) is shown in Figure 15 which shows that RATRAN produces a line profile with a larger contrast between the temperature of the blue peak and the minimum between the red and blue peaks (so a larger value of D_r , Appendix A) than either LIME or RADMC-3D. The infall velocity from LIME and inferred by Hill5 map are in good agreement, although Hill5 implies a smaller velocity dispersion.

4.3 The Spatial Distribution of Line Profiles

For the LIME models which fit the central pixel spectra best among their own series of parameters, we also compare the spatial distribution of the models with the data. The spatial distribution of R statistic in those models is summarised in Figure 16. For this comparison, the effective telescope efficiency is calculated for each pixel which allows for possible unresolved changes in the structure of the clump.

Overall, in the central regions, all the models appear to provide reasonable fits to the observations, although models that have infall velocities that decrease with radius ($f < 1$) appear to produce slightly worse agreement (fitting a smaller number of pixels with small R values) than models with uniform or increasing ($f \geq 1$) infall velocity. However, the models that have infall velocities that increase with radius ($f > 1$) provide fits with lower R values to the emission to the north of the map.

Figure 17 shows the region of Figure 5 where $r < 2.7 \times 10^{18} \text{ cm}$ with the results of Hill5 fits for v_{in} ($v_{in,Hill5}$) to individual pixels in

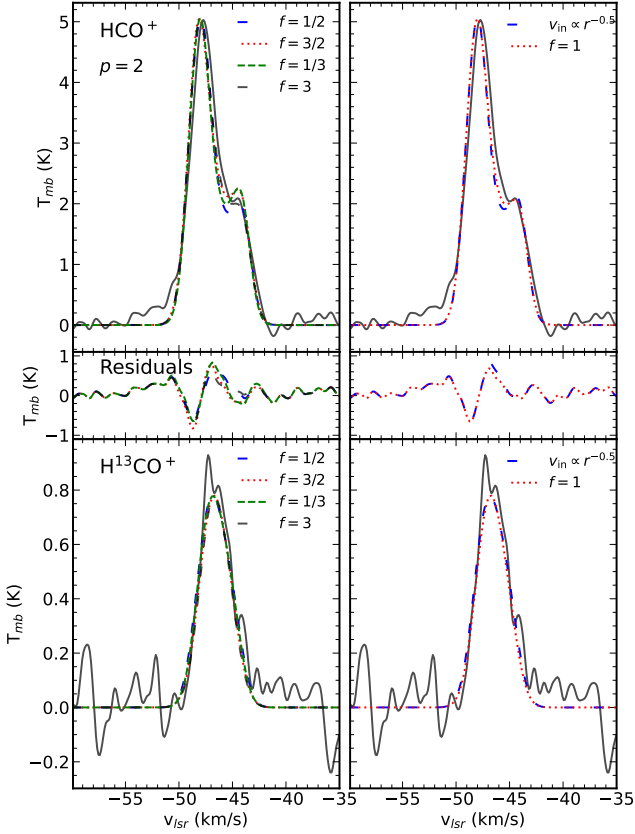


Figure 12. The central pixel $\text{HCO}^+ J=1-0$ and $\text{H}^{13}\text{CO}^+ J=1-0$ profiles from different best fit models with a $p=2$ density profile compared to the observational data. The top row shows a comparison of six models with different infall velocity profiles. The parameters of these models are given in Table 3. The middle row shows the difference between each model and observations. The bottom row shows the predicted H^{13}CO^+ from these same models compared with the observed H^{13}CO^+ emission.

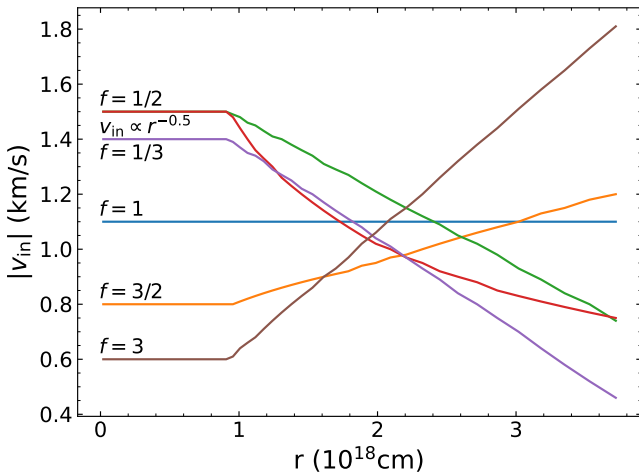


Figure 13. Velocity profiles of the models with $p=2$ which give the best fit to the central pixel.

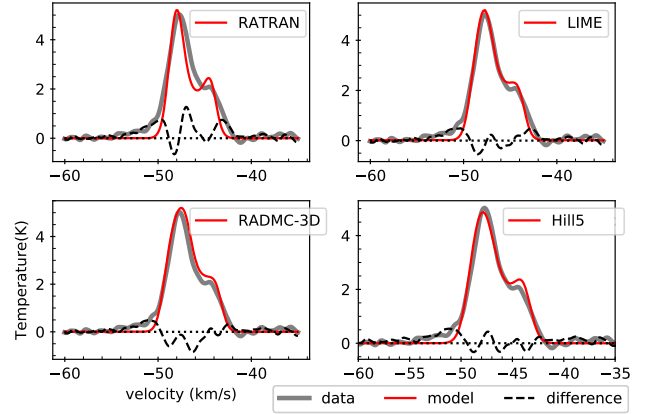


Figure 14. The central pixel line profiles from different models compared to the observational data. The light gray lines represent the $\text{HCO}^+ J=1-0$ data at the central pixel. The red lines are the central pixel profiles from models. The dashed black lines represent the differences between the models and observational data. The dotted horizontal lines represent where the differences are zero. The profiles of RT modelling (RATRAN, LIME, and RADMC-3D) are fitted to the telescope main beam efficiency and normalised to fit to the data.

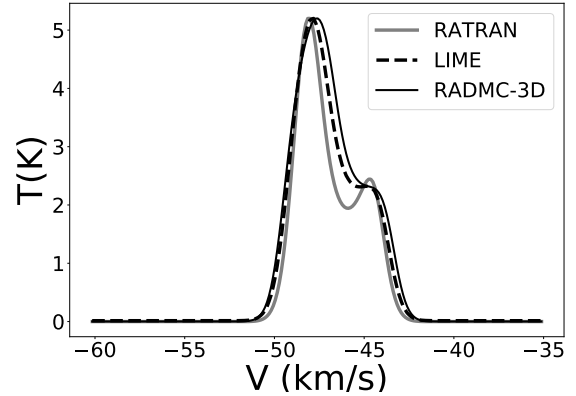


Figure 15. Comparison of the model central pixel spectra from RATRAN, LIME, and RADMC-3D for the best fit values in Table 3 for a temperature of 20 K. The models, i.e., $M_{\text{LIME},7}$, M_{RADMC3D} , and M_{RATRAN} have all been normalised to the peak intensity of the observed line.

the HCO^+ cube together with the binned average of these values. In addition, the values of v_{in} determined by Hill5 fits to spectrum at the central pixel, and averaged over the two annular regions A1 and A2 (Table 2) are shown. All three of these estimates of v_{in} are in good agreement, showing a decrease in the magnitude of v_{in} from about 1.2 km s^{-1} at the centre of the map to $\sim 0.5 \text{ km s}^{-1}$ at a radius of $2.2 \times 10^{18} \text{ cm}$ ($45''$). The solid curves on the figure show the result of Hill5 fitting to the central pixel and the annular regions for the $p=2.0$, $f=1/3$, 1 and 3 models ($M_{\text{LIME},4}$, $M_{\text{LIME},6}$, and $M_{\text{LIME},10}$) which provide the best fit to the central pixel. Although only one of these models has an infall velocity that actually decreases with radius (the model with $f=1/3$ ($M_{\text{LIME},4}$)), the Hill5 fits for all three models show a decrease in the fitted infall velocity with radius, all approximately consistent with the observations. For the same values of f , other models with slightly different velocities and dispersions

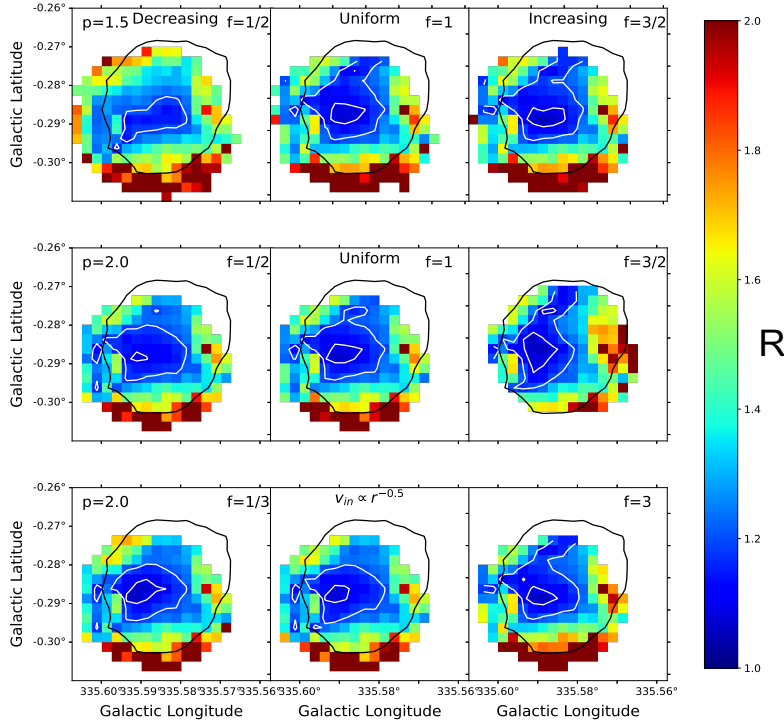


Figure 16. The spatial distribution of the R statistic in the best fit models and observations. The top row shows models with $p = 1.5$ and the other two rows models with $p = 2.0$. The columns show models with f from a decreasing v_{in} profile ($f < 1$, in the left columns), a uniform v_{in} (the middle columns), and an increasing v_{in} profile ($f > 1$, the right columns). The white contours show $R = 1.1$ and 1.2 , and the single black contour shows where the integrated intensity of the emission over the velocity range used to calculate P_r is 20% of its peak intensity.

(and so slightly worse fits to the central pixel) can come closer to the observed values and trend.

The apparent consistency of these different models shows that the apparent decrease in v_{in} inferred by Hill5 for the observations does not necessarily reflect an actual decrease in the infall velocity. Rather this decrease is likely a result of a combination of decreasing optical depth and geometry leading to a less asymmetric line profile and resulting in Hill5 inferring a lower v_{in} .

4.4 H^{13}CO^+

Observations of $\text{H}^{13}\text{CO}^+ J=1-0$ can also provide information about the spatial variation in the infall velocity profile. Its lower optical depth, due to its lower abundance than the main isotopologue, results in this species not having a significant blue asymmetric line profile. On the other hand, systematic motions such as due to infall, should be reflected in the width of the line. However, due to weakness of the line and so the low signal to noise ratio in the Mopra observations, analysis of the existing data is limited to the study of the radial profile of the H^{13}CO^+ line width, rather than its full spatial distribution over the region.

Figure 18 (left) shows the FWHM of $\text{H}^{13}\text{CO}^+ J=1-0$ derived from Gaussian fits to the observed spectra at the central pixel and in the three annular regions around the central pixel (Table 2). The FWHM peaks towards the central pixel while at larger radii it is smaller, but remarkably uniform at $\sim 3.1 \text{ km s}^{-1}$ even out to $65''$ from the central source. This is clearly shown in the right-hand panel of the figure which shows the normalised H^{13}CO^+ spectra in the

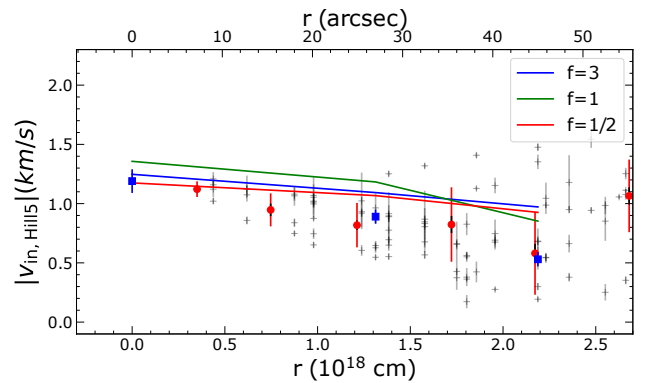


Figure 17. Infall velocity v_{in} ($v_{\text{in,Hill5}}$) from Hill5 fitted spectra as a function of radius from the central pixel. The grey and red points are as shown in Figure 5. The three blue points show the result of Hill5 fits to the observations at the central pixel and the observations averaged over the two annular regions A1 and A2. The three colour lines connect the Hill5 fits to the annular average spectra at three radii (the central pixel and the spectra averaged over the two annular regions A1 and A2) from the best fit models for $f = 1/2, 1$ and 3 (models $M_{\text{LIME},5}$, $M_{\text{LIME},6}$ and $M_{\text{LIME},10}$ respectively).

annular regions. Comparing the observed H^{13}CO^+ widths with the intrinsic velocity width of the gas in the models (as shown by the gray-shaded region on Figure 18 (left) and the width expected for models with no infall (the gray-dashed curves), the figure shows that at all positions the H^{13}CO^+ has a line width greater than the

width necessary to fit the HCO^+ emission. This points to the infall motions in the clump making a significant contribution to the width of the H^{13}CO^+ emission.

The variation of the predicted H^{13}CO^+ line width with radius from the models with infall is shown by the coloured curves demonstrating the impact of the infall on this line. All the infall models show a decrease in line width with increasing radius, but the models in which the infall velocity decreases with radius ($f = 1/2$ and $f = 1/3$) show the steepest decrease with radius. At the outer edge of these models, the line width falls to close to the intrinsic velocity width in the models. Although these models match the central line width and the decrease at $28''$, they can not reproduce the uniform line width beyond $28''$.

Models where the infall velocity is uniform, or increases with radius ($f = 1$ and 3) show a slower decrease in the width of H^{13}CO^+ with increasing radius, with the $f = 3$ model showing a variation of only a little more than 0.1 km s^{-1} over the full range of radius. Although this model does not match the large width at the centre as closely as $f = 1$ and $1/2$ models do, the $f = 3$ model comes closest to matching the near uniform observed line width away from the centre.

In summary, infall appears to make a significant contribution to the observed line widths of H^{13}CO^+ $J = 1 - 0$. Models with a decrease in v_{in} out to $\sim 30''$ match the drop in line width close to the central source, however models where the infall velocity is uniform or increasing with radius best match the observed spatial distribution of the H^{13}CO^+ line width at the largest radii.

5 DISCUSSION

5.1 The Impact of The Density Profile

Our models show that the assumed density profile ($p = 1.5$ or $p = 2.0$) has a relatively small impact on the best fit infall velocity for a given variation of the infall velocity with radius. For the uniform infall velocity case ($f = 1$), for both models with a constant temperature (20 K, $M_{\text{LIME},2}$ and $M_{\text{LIME},7}$) and those with a temperature profile ($M_{\text{LIME},1}$ and $M_{\text{LIME},6}$), the best fit values for v_{in} are the same for both density profiles. For a uniform temperature of 20 K ($M_{\text{LIME},2}$ and $M_{\text{LIME},7}$), the infall velocity is -1.3 km s^{-1} and $\Delta v_b = 1.5 \text{ km s}^{-1}$ while models with a temperature profile ($M_{\text{LIME},1}$ and $M_{\text{LIME},6}$) have a somewhat smaller infall velocity (-1.1 km s^{-1}) and slightly larger $\Delta v_b = 1.6 \text{ km s}^{-1}$. There is a similar difference of 0.2 km s^{-1} in v_{in} for the two density profiles for models with $f = 1/2$ and $f = 3/2$ ($M_{\text{LIME},0}$ and $M_{\text{LIME},5}$ for $f = 1/2$, and $M_{\text{LIME},3}$ and $M_{\text{LIME},9}$ for $f = 3/2$ in Table 3). The choice of density profile does, however, impact the predicted line strength. For example, comparing the $f = 1$ models $M_{\text{LIME},1}$ and $M_{\text{LIME},6}$, the model with $p = 2$, $M_{\text{LIME},6}$, has a central line peak intensity of 8.7 K compared with 7.5 K for the model with $p = 1.5$, $M_{\text{LIME},1}$.

5.2 Infall Velocity Profile

Applying Hill5 to the HCO^+ $J = 1 - 0$ cubes produces a map of the inferred v_{in} which suggests that close to the source, the infall velocity decreases with increasing distance from the source. However, comparison with radiative transfer models shows this apparent decrease can be consistent with a range of radially varying infall velocity, from decreasing to increasing with radius (Sec. 4.3). The degeneracy between these models could however be broken with observations of additional transitions of HCO^+ . As an example,

Table 4. Results from applying Hill5 to the central spectra from the 20 K RT models ($M_{\text{LIME},2}$ and $M_{\text{LIME},7}$) shown in Table 3.

Infall parameters	RATRAN	LIME	RADMC-3D
σ (km s^{-1})	1.06 ± 0.01 (1.13)	1.02 ± 0.02 (1.06)	1.02 ± 0.01 (1.30)
$v_{\text{in,Hill5}}$ (km s^{-1})	-0.80 ± 0.02 (0.9)	-1.16 ± 0.04 (1.30)	-1.21 ± 0.03 (1.60)

Notes. The values in brackets indicate the actual values from the models in Table 3.

Figure 19 shows a comparison of the $J = 1 - 0$ transition towards the centre of the three models shown in Figure 17. Compared with the $J = 1 - 0$ transitions, the $J = 3 - 2$ transitions show a stronger blue asymmetry. This is the result of the difference in the excitation of the transitions plus the smaller telescope beam used to convolve the models ($22''$ for the $J = 3 - 2$ transition, representative of the beam of the 12-m diameter APEX telescope compared with the $37''$ for the $J = 1 - 0$ transition.). The figure shows that the infall velocity estimated by Hill5 from the $J = 1 - 0$ transitions differs at most by 0.12 km s^{-1} between the models. On the other hand, higher angular resolution observations of the $J = 3 - 2$ transition seem to provide a better discrimination between the models, with the magnitude of the infall velocities ranging from 0.86 km s^{-1} to 1.25 km s^{-1} , a range of 0.39 km s^{-1} .

As discussed in Section 4.4, infall motions affect the line width of the optically thinner H^{13}CO^+ $J = 1 - 0$. If the line width at the centre of the clump is not significantly impacted by other motions, such as the impact of the outflows from the embedded sources, the decrease in line width from 3.5 km s^{-1} , at the centre of the clump to $\sim 3.1 \text{ km s}^{-1}$ at larger radii seen in Figure 18 would appear most consistent with a model where the infall velocity is greatest closer to the embedded sources. However, the uniform line width at larger distances suggests higher infall velocities at these larger distances. Note that, except at the central position, these line widths are measured in spectra averaged over annular regions and so sample relatively large volumes of the clump, meaning that they are unlikely to have significant contributions from outflows as the outflows are of limited spatial extent (Avison et al. 2021). Also, the clump is seen in absorption at $8 \mu\text{m}$ (Peretto et al. 2013), indicating that it has not been strongly disrupted by outflows, which would otherwise reduce the extinction and allow near-infrared emission to escape.

5.3 Hill5 Model Sensitivity and Accuracy

The Hill5 method was developed for the emission from regions where $|v_{\text{in}}| < \sigma_v$ but it can give good estimates of infall velocity when σ_v and v_{in} are comparable (De Vries & Myers 2005; Barnes et al. 2010). However, it has been suggested that the ‘Hill’ method underestimates the actual infall velocities in a region in some circumstances (e.g. Walsh et al. 2006). A possible reason could be that the ‘Hill’ model, as well as its precursor ‘two-layer’ model, do not take into account the portion of the cloud whose systematic line-of-sight velocity is zero (Walsh et al. 2006).

Applying Hill5 to the central pixel of the observations indicates an infall velocity of -1.2 km s^{-1} , within 0.1 km s^{-1} of the best fit uniform infall velocity models which give -1.3 km s^{-1} for $T = 20 \text{ K}$ ($M_{\text{LIME},2}$ and $M_{\text{LIME},7}$) and -1.1 km s^{-1} for models with a temperature profile ($M_{\text{LIME},1}$ and $M_{\text{LIME},6}$). Hill5 fits a velocity dispersion of 1.05 km s^{-1} identical to the 20 K models, but lower than the 1.13 km s^{-1} of the temperature profile models, although this difference is likely not significant. Table 4 and Figure 20 show the results of applying Hill5 to the output of the uniform v_{in} radiative transfer models. Although Hill5 can fit the line profiles (Figure 20), it results in an underestimate of both the infall velocity and dispersion compared with the input values for all three models. This is

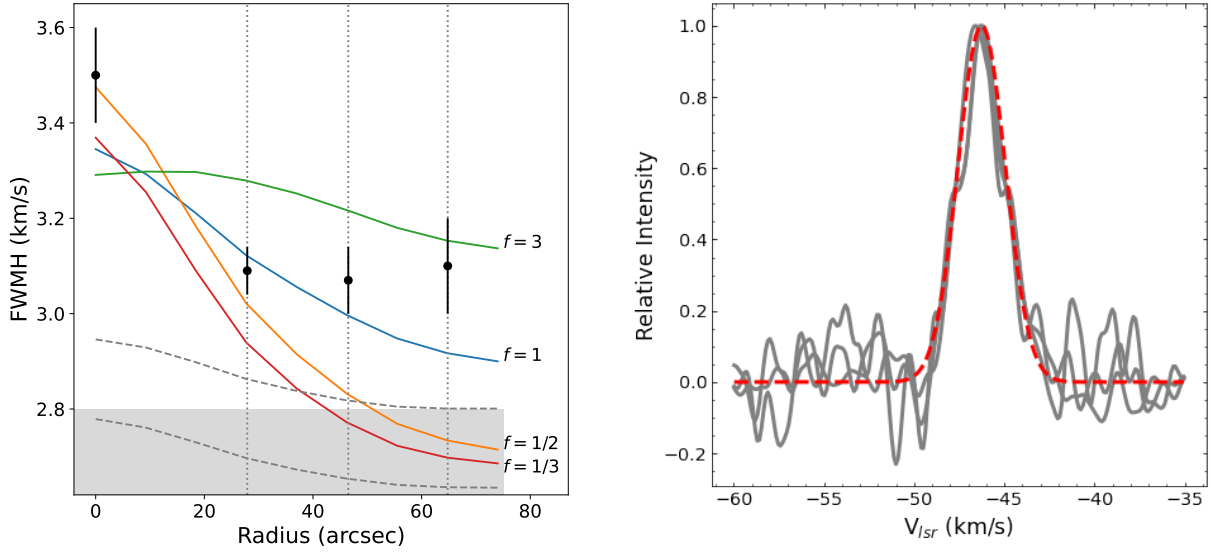


Figure 18. *Left:* The variation of the width of the H^{13}CO^+ $J=1-0$ line for models with different v_{in} radial structures. The $p=2$ best fit models are shown, labelled by the f value for the model. The vertical dotted lines show the radii of the annular apertures used to average the observed spectra shown in the accompanying plot. The black points and error bars show the observed FWHM and their uncertainties determined from Gaussian fits to the H^{13}CO^+ $J=1-0$ line at the centre of the map and the annular average spectra. The gray-shaded region shows the range of the intrinsic velocity dispersion (expressed as FWHM) for the infall models shown. The dashed gray curves show the FWHM of the line from two static models (models with no infall), demonstrating the expected variation in the absence of infall. The velocity dispersion in these models was selected to span the range of values in the models shown by the coloured curves. *Right:* The observed H^{13}CO^+ $J=1-0$ averaged over the annular regions with mid-point radius shown on the panel to the left (grey). The red dashed curve shows the Gaussian fit to the spectrum at radius $65''$.

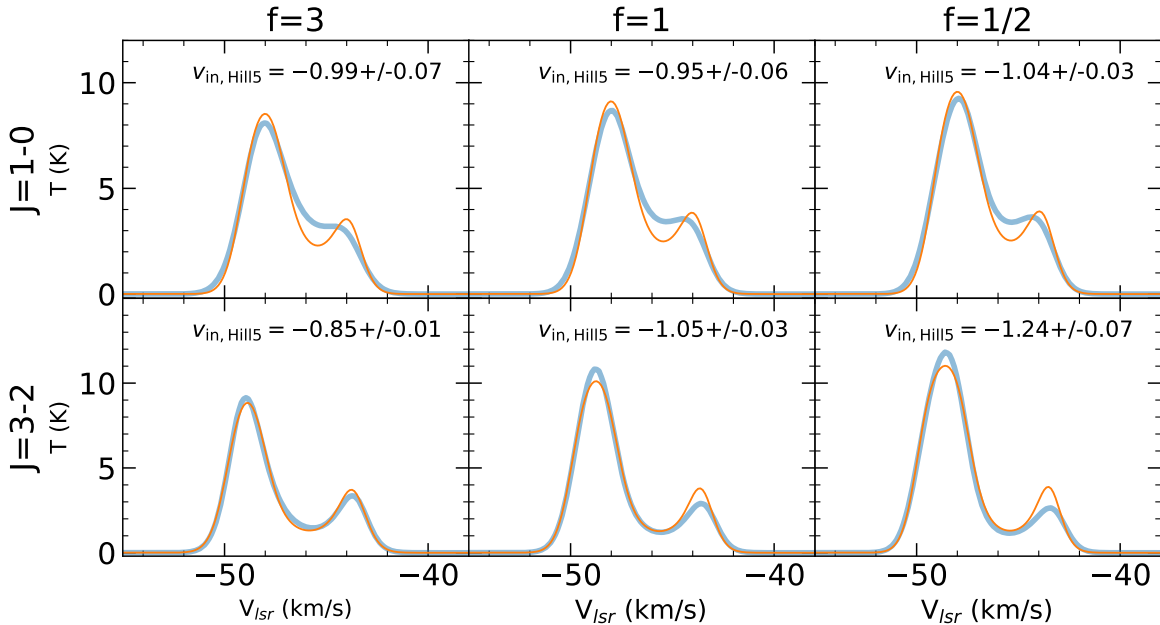
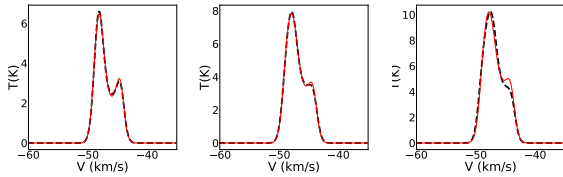


Figure 19. Comparison of the HCO^+ $J=1-0$ (upper) and $J=3-2$ (lower) spectra towards the central pixel of the LIME $f=3$ (left), $f=1$ (middle) and $f=1/2$ (right) models ($M_{LIME,10}$, $M_{LIME,6}$, and $M_{LIME,5}$, respectively). The broad, blue curve in each panel shows the model spectrum and the thinner orange curve, the Hill5 fit to the spectrum. The Hill5 fitted infall velocity and its uncertainty are shown in the upper right of each panel. Note that for these fits no noise was added to the model spectra. The model $J=3-2$ spectra have been convolved with a $22''$ FWHM beam and while the $J=1-0$ transitions have been convolved with the $37''$ beam of the observations.

Table 5. Weighted infall velocities for the best-fitting $p = 2$ models with the most extreme values of f .

f	v_c (km s^{-1})	$\bar{v}_{\text{in,m}}$ (km s^{-1})	$\bar{v}_{\text{in},\rho}$ (km s^{-1})
1/3	-1.70	-0.98	-1.08
3	-0.60	-0.87	-0.38

Notes. v_c is the infall velocity in the central region defined in equation (4); $\bar{v}_{\text{in,m}}$ is the mass-weighted infall velocity over the entire clump; and $\bar{v}_{\text{in},\rho}$ is the density-weighted line-of-sight infall velocity towards the clump centre. These values can be compared with the Hill5 fits to the central spectrum listed in Table 1.

**Figure 20.** Hill5 model fitting to the RT models. From left to right are RATRAN, LIME, and RADMC-3D results represented by the black dashed lines. The red profiles are the Hill5 fitting to the models.

consistent with Kirk et al. (2013), who argue that the results from Hill5 fitting should only be considered as a lower limit to the infall velocity.

This discrepancy can be larger when Hill5 is applied to models with non-uniform v_{in} . For models where the infall velocity varies with radius (Table 3), depending on the form of this variation, Hill5 can either significantly underestimate or overestimate the infall velocity at centre of the clump. Towards the central position, Hill5 gives an infall velocity of -1.2 km s^{-1} whereas models with central infall velocities as extreme as -0.60 and -1.60 km s^{-1} can fit the observations (with different radial variations of the infall velocity). For comparison, Table 5 presents the mass- and density-weighted infall velocities for these extreme models, providing representative line-of-sight averaged velocities for both increasing and decreasing radial infall profiles. Comparing with the results in Table 1 shows that Hill5 overestimates the infall velocity compared with these line-of-sight ‘averaged’ values. Despite these shortcomings, in situations where models of the infall are not readily available, Hill5 provides a useful (and widely used) method to parameterise the infall velocity. However, as the exploration of the infall structure here shows, the results need to be interpreted with caution.

5.4 Implications for massive star formation

Different from low-mass star formation, where infall velocities are found to be around -0.5 km s^{-1} (e.g. Walsh et al. 2006; Kirk et al. 2013), massive star formation is found with higher infall velocities around $\sim -1.5 \text{ km s}^{-1}$ (e.g. Klaassen et al. 2012; Rygl et al. 2013; Contreras et al. 2018; Neupane et al. 2020). With a larger infall velocity, assuming a constant accretion throughout the formation, individual clump gains mass quicker in high-mass star-forming scenario than in lower-mass counterparts.

For massive star precursors, the accretion rates are greater than lower-mass counterparts, with the value from $\times 10^{-4}$ to up to a few $\times 10^{-3} M_{\odot} \text{ yr}^{-1}$ (e.g. Fuller et al. 2005; Klaassen et al. 2012). The previous calculation of infall velocity from Peretto et al. (2013) estimated an accretion rate in SDC335 of $(2.5 \pm 1.0) \times 10^{-3} M_{\odot} \text{ yr}^{-1}$ on the clump scale and Avison et al. (2021) have shown that the young

outflows from the embedded protostars in SDC335 imply similar high values close to the protostars. Using an angular resolution of $0.3''$ (corresponding to 1000 AU), Olguin et al. (2021) used red-shifted absorption of $^{13}\text{CO J} = 2 - 1$ to estimate an infall velocity of -1.7 km s^{-1} with respect to a systemic velocity of -46.9 km s^{-1} , which would correspond to an infall velocity of -1.3 km s^{-1} with respect to the -46.5 km s^{-1} adopted here. This is broadly consistent with recent ALMA results indicating that, on still smaller scales, the gas kinematics can reflect a transition between a rotating disc and a rotating, infalling envelope, with anisotropic accretion feeding the central protostellar system (Olguin et al. 2026). Due to the low critical density and high optical depth of $^{13}\text{CO J} = 2 - 1$, Olguin et al. (2021) argued this traces the infall on a large size scale (rather than close to the central source) which would be consistent with the large infall velocities at large radius our results suggest. From the models here it is possible to describe the implied mass inflow rates as a function of radius in the clump. These are shown for the best fit models in Figure 21. The values are mostly in the range $10^{-3} M_{\odot} \text{ yr}^{-1}$ to $10^{-2} M_{\odot} \text{ yr}^{-1}$ with the spatial variation depending on the assumed density and infall velocity profile. Notice that the density profile has a significant impact on the range of the implied mass inflow rates.

The inverted infall velocity structure, larger infall velocity at larger radii, implied by our three-dimensional RT modelling of SDC335 means that the mass flux has to be larger at larger radii. Such a configuration prevents any simple continuous mass flow toward the cloud centre. Infalling material will have to pile up or otherwise form structures at some intermediate scales, i.e. between the infall/cloud scales of $\sim 1 \text{ pc}$ and the dense core scale of $\lesssim 0.1 \text{ pc}$. Thus, our model of the pc-scale infall suggest that fragmentation or the formation of filamentary structures will happen at intermediate scales for this massive star-forming region, as indeed is seen in higher resolution observations of this region (Xu et al. 2023b).

5.5 The origin of non-thermal motions

There has long been discussion of the origin of the supra-thermal line widths observed in molecular gas (e.g. Zuckerman & Evans 1974; Myers et al. 1983; Hacar et al. 2016) and how their variation with size may trace the turbulent cascade of energy between size scales (e.g. Ballesteros-Paredes et al. 2011; Chira et al. 2019; Vázquez-Semadeni et al. 2019). More recently, Traficante et al. (2020) suggested that the relatively shallow variation of observed line width with size when moving from their environment down to $\sim \text{pc}$ -scale clumps, especially in high mass and high surface density regions, is a consequence of a contribution from infall to the line width and in SPH simulations of a collapsing clump by Peretto et al. (2007) the line broadening was dominated by the collapse. Based on the relationship between velocity dispersion, size, and surface density for a sample of $70 \mu\text{m}$ quiet clumps, Traficante et al. (2018a) presented a similar interpretation. Using maps of a sample of IRDCs, Peretto et al. (2023) have shown that the spatial profile of the velocity dispersion shows an abrupt flattening in slope when transitioning from clouds to their denser, parsec-scale, inner regions (clumps). After decreasing towards smaller size scales in the envelope, the velocity dispersion (as traced by $\text{N}_2\text{H}^+ \text{ J} = 1 - 0$) is uniform across the clumps. This is interpreted as the pc-scale clumps being dynamically decoupled from their envelopes and suggesting the clumps are dominated by gravitational motions.

As Figure 18 shows (Sec. 4.4), away from the central source, $\text{H}^{13}\text{CO}^+ \text{ J} = 1 - 0$ in SDC335 has a uniform distribution line width, similar to $\text{N}_2\text{H}^+ \text{ J} = 1 - 0$ in the sources observed by Peretto et al.

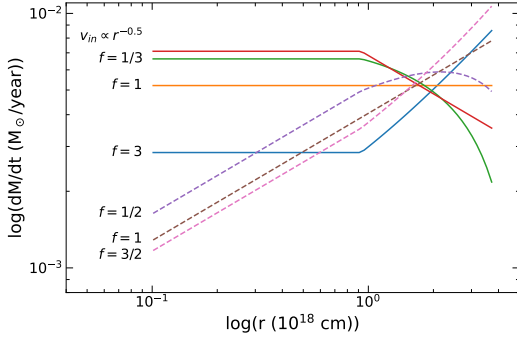


Figure 21. Mass accretion rates as a function of radius within the clumps for the best fit models of SDC335. The dashed curves show models with $p = 1.5$ and the solid curves, models with $p = 2$. The curves are labelled with the f or the form of the infall velocity.

(2023) and that infall can be responsible for this behaviour. Simulations suggest that the infall contribution to the observed velocity dispersion should be common in cores (~ 0.1 pc-size regions) (e.g. Ballesteros-Paredes et al. 2018; Ntormousi & Hennebelle 2019) and supersonic line widths have been considered to trace the gravitational collapse where a virial-like relation developed from the gravity release (e.g. Ballesteros-Paredes et al. 2011; Ramfrez-Galeano et al. 2022), which is consistent with the enlarged line widths contributed from infall in our models. Our models demonstrate the significant contribution of infall to the observed line widths of an optically thin dense gas tracer in massive clumps as was also seen in the simulations of Peretto et al. (2007). This was also suggested by the ALMA core-scale study of Morii et al. (2025). This opens the possibility of using the line widths of optically thin tracers to trace infall. In addition, the previously poorly recognised contribution to the line width from infall can significantly affect the interpretation of the virial parameter, and hence the interpreted stability of clumps (e.g. Ballesteros-Paredes 2006; Traficante et al. 2018c,b; Singh et al. 2021).

6 CONCLUSIONS

We have carried out a systematic study of the infall in SDC335, a prototypical massive star-forming IRDC using the semi-analytical Hill5 model and radiative transfer models to study the emission of HCO^+ . Focusing on models using LIME, we have explored the spectral line profiles produced by different infall velocity structures. Our main results are:

(i) A range of infall velocity structures can reproduce the blue asymmetric $\text{HCO}^+ J=1-0$ line profile at the centre of the map with the best fit infall velocity in the central regions dependent on the assumed structure of the infall velocity in the outer regions of the clump.

(ii) In the central region of the clump SDC335 (at a radius of $< 9.3 \times 10^{18}$ cm, < 0.3 pc), the magnitude of the infall velocities is constrained within a factor of ~ 3 to be between 0.6 and 1.6 km s^{-1} , with a weak dependence on the assumed cloud conditions, such as the density profile or temperature.

(iii) The observed spectra show evidence of infall out to radii of $\sim 6 \times 10^{18}$ cm (1.95 pc). Fitting the spectra with Hill5 shows a central peak in the inferred magnitude of the infall velocity of about 1.2 km s^{-1} , followed by a decrease to about 0.6 km s^{-1} at

a radius $\sim 2 \times 10^{18}$ cm (0.65 pc). At larger distances, Hill5 infers infall velocities $\sim -1 \text{ km s}^{-1}$.

(iv) Radiative transfer models show that the apparent decrease in the magnitude of the infall velocity inferred from Hill5 fits to $\text{HCO}^+ J=1-0$ does not uniquely imply that the actual infall velocity is decreasing with increasing radius. For example, such a decrease can be reproduced with models in which the velocity of the infalling gas is greater at 2×10^{18} cm (0.65 pc) than at the centre of the clump. Radiative transfer models show that the degeneracy between different structures for the infall velocity which can reproduce the structure seen in $\text{HCO}^+ J=1-0$ could be broken with observations of additional HCO^+ transitions.

(v) Outside the central region, the line width of $\text{H}^{13}\text{CO}^+ J=1-0$ line is surprisingly constant. Comparison with synthetic spectra from our radiative transfer models show that this uniform line width has a significant contribution from unresolved infall motions over the entire clump. Typically, the line width in clumps is interpreted as due to turbulence, so this contribution from infall can significantly impact and alter our interpretation of the energetics and dynamical state of clumps.

(vi) Combining the comparison of the observed HCO^+ and H^{13}CO^+ emission with the radiative transfer models favours an interpretation where the magnitude of the infall velocity is a maximum of $\sim 1.5 \text{ km s}^{-1}$ towards centre of the clump and then decreases by a factor of 0.8 to about 1.2 km s^{-1} at $\sim 2 \times 10^{18}$ cm ($\sim 40''$) (Figure 18). Then at larger radii, the magnitude of the infall velocity is uniform or somewhat increasing with values of ~ 1.3 to 1.6 km s^{-1} at a distance of $\sim 4 \times 10^{18}$ cm (1.30 pc), consistent with the results of Olguin et al. (2021).

(vii) The implied pc-scale mass inflow rates were found to be between 3×10^{-3} and $10^{-2} M_{\odot} \text{ yr}^{-1}$. Clearly, the internal structure of SDC335 is in reality significantly more complex than the simple spherical models used here. However, given the high optical depth and spatial extent of the $\text{HCO}^+ J=1-0$ emission, the impact of such structure is difficult to assess without high angular resolution observations which sample the full range of size scales. Nevertheless, this first exploration of models applied to spatially extended infall signatures demonstrates the ability of modelling to constrain (the spherically averaged) infall properties in the region.

With the ever increasing volume of spatially-resolved infall signatures, modelling the line profiles on such spectral maps holds the promise to shed significant light on the dynamics of pc-scale infall.

ACKNOWLEDGEMENTS

We want to thank the anonymous referee for his or her constructive suggestions, which have greatly improved this paper. This work is supported by the National Natural Science Foundation of China grant No. 12588202, the International Partnership Program of the Chinese Academy of Sciences grant No. 114A11KYSB20210010, the National Key R&D Program of China No. 2022YFA1603103, Tianshan Talent Training Program 2024TSYCTD0013, and Natural Science Foundation of Xinjiang Uygur Autonomous Region No. 2025D01B173. It was also partially funded by the Regional Collaborative Innovation Project of Xinjiang Uygur Autonomous Region grant 2022E01050, Tianshan Talent Training Program, and Tianchi Talent Project of Xinjiang Uygur Autonomous Region. X.J.J. acknowledges the support by the Chinese Scholarship Council (CSC) and the STFC China SKA Exchange Programme for support as a visiting PhD student in the United Kingdom. X. J. J. wants to thank Xu Dan and her Xiao Dan Gao. X. J. J. also wants to thank

Dr. Qianru He and Xiale (Ruilin Xia) for the help on this paper. G.A.F acknowledges financial support from the State Agency for Research of the Spanish MCIU through the AYA 2017-84390-C2-1-R grant (co-funded by FEDER) and through the "Center of Excellence Severo Ochoa" award for the Instituto de Astrofísica de Andalucía (SEV-2017-0709). G.A.F also acknowledges support from the Collaborative Research Centre 956, funded by the Deutsche Forschungsgemeinschaft (DFG) project ID 184018867. G.A.F also gratefully acknowledges the DFG for funding through SFB 1601 "Habitats of massive stars across cosmic time" (sub-project B1) and from the University of Cologne and its Global Faculty programme. J. W thanks to the support of the Tianchi Talent Program of Xinjiang Uygur Autonomous Region. This research made use of Astropy (<http://www.astropy.org>), a community-developed core Python package for Astronomy (Astropy Collaboration et al. 2013, 2018, 2022) as well as the related packages Pyspeckit (Ginsburg et al. 2022; Ginsburg & Mirocha 2011) and spectral-cube (Ginsburg 2016; Ginsburg et al. 2019).

Facilities: ATNF Mopra 22m

Software: RADMC-3D, RATRAN, LIME, idl, Astropy, Pyspeckit, spectral-cube

Data Availability

The data analysed in this paper are available from <https://atoa.atnf.csiro.au/MALT90>.

REFERENCES

- Anglada G., Rodríguez L. F., Canto J., Estalella R., Lopez R., 1987, *A&A*, **186**, 280
- Astropy Collaboration et al., 2013, *A&A*, **558**, A33
- Astropy Collaboration et al., 2018, *AJ*, **156**, 123
- Astropy Collaboration et al., 2022, *ApJ*, **935**, 167
- Avison A., Peretto N., Fuller G. A., Duarte-Cabral A., Traficante A., Pineda J. E., 2015, *A&A*, **577**, A30
- Avison A., et al., 2021, *A&A*, **645**, A142
- Ballesteros-Paredes J., 2006, *MNRAS*, **372**, 443
- Ballesteros-Paredes J., Hartmann L. W., Vázquez-Semadeni E., Heitsch F., Zamora-Avilés M. A., 2011, *MNRAS*, **411**, 65
- Ballesteros-Paredes J., Vázquez-Semadeni E., Palau A., Klessen R. S., 2018, *MNRAS*, **479**, 2112
- Barnes P. J., Yonekura Y., Ryder S. D., Hopkins A. M., Miyamoto Y., Furukawa N., Fukui Y., 2010, *MNRAS*, **402**, 73
- Beuther H., Schilke P., Menten K. M., Motte F., Sridharan T. K., Wyrowski F., 2002, *ApJ*, **566**, 945
- Bjerkeli P., et al., 2023, *A&A*, **677**, A62
- Brinch C., Hogerheijde M. R., 2010, *A&A*, **523**, A25
- Calahan J. K., et al., 2018, *ApJ*, **862**, 63
- Chira R. A., Ibáñez-Mejía J. C., Mac Low M. M., Henning T., 2019, *A&A*, **630**, A97
- Churchwell E., et al., 2009, *PASP*, **121**, 213
- Contreras Y., et al., 2018, *ApJ*, **861**, 14
- De Vries C. H., Myers P. C., 2005, *ApJ*, **620**, 800
- Dullemond C. P., Juhasz A., Pohl A., Sereshii F., Shetty R., Peters T., Commercon B., Flock M., 2012, RADMC-3D: A multi-purpose radiative transfer tool, Astrophysics Source Code Library, record ascl:1202.015 (ascl:1202.015)
- Elmegreen B. G., Lada C. J., 1977, *ApJ*, **214**, 725
- Evans Neal J. I., Di Francesco J., Lee J.-E., Jørgensen J. K., Choi M., Myers P. C., Mardones D., 2015, *ApJ*, **814**, 22
- Foster J. B., et al., 2011, *ApJS*, **197**, 25
- Foster J. B., et al., 2013, *Publ. Astron. Soc. Australia*, **30**, e038
- Fuller G. A., Williams S. J., Sridharan T. K., 2005, *A&A*, **442**, 949
- Ginsburg A., 2016, A quick overview of radio-astro-tools, doi:10.5281/zenodo.48189, <https://doi.org/10.5281/zenodo.48189>
- Ginsburg A., Mirocha J., 2011, PySpecKit: Python Spectroscopic Toolkit, Astrophysics Source Code Library, record ascl:1109.001 (ascl:1109.001)
- Ginsburg A., et al., 2019, radio-astro-tools/spectral-cube: Release v0.4.5, doi:10.5281/zenodo.3558614, <https://doi.org/10.5281/zenodo.3558614>
- Ginsburg A., Sokolov V., de Val-Borro M., Rosolowsky E., Pineda J. E., Sipőcz B. M., Henshaw J. D., 2022, *AJ*, **163**, 291
- Gómez G. C., Vázquez-Semadeni E., Palau A., 2021, *MNRAS*, **502**, 4963
- Hacar A., Alves J., Burkert A., Goldsmith P., 2016, *A&A*, **591**, A104
- He Y.-X., et al., 2023, *ApJ*, **957**, 61
- Hogerheijde M. R., van der Tak F. F. S., 2000, *A&A*, **362**, 697
- Hosokawa T., Omukai K., 2009, *ApJ*, **691**, 823
- Hosokawa T., Yorke H. W., Omukai K., 2010, *ApJ*, **721**, 478
- Jackson J. M., et al., 2013, *Publ. Astron. Soc. Australia*, **30**, e057
- Jackson J. M., et al., 2019, *ApJ*, **870**, 5
- Jackson J. M., et al., 2026, *ApJ*, **998**, 167
- Jacobsen S. K., Jørgensen J. K., Di Francesco J., Evans N. J., Choi M., Lee J.-E., 2019, *A&A*, **629**, A29
- Kirk H., Myers P. C., Bourke T. L., Gutermuth R. A., Hedden A., Wilson G. W., 2013, *ApJ*, **766**, 115
- Klaassen P. D., Testi L., Beuther H., 2012, *A&A*, **538**, A140
- Ladd N., Purcell C., Wong T., Robertson S., 2005, *Publ. Astron. Soc. Australia*, **22**, 62
- Lee C. W., Myers P. C., Tafalla M., 2001, *ApJS*, **136**, 703
- López-Sepulcre A., Cesaroni R., Walmsley C. M., 2010, *A&A*, **517**, A66
- Morii K., Sanhueza P., Csengeri T., Nakamura F., Bontemps S., Garay G., Zhang Q., 2025, *ApJ*, **979**, 233
- Myers P. C., Linke R. A., Benson P. J., 1983, *ApJ*, **264**, 517
- Myers P. C., Bachiller R., Caselli P., Fuller G. A., Mardones D., Tafalla M., Wilner D. J., 1995, *ApJ*, **449**, L65
- Myers P. C., Mardones D., Tafalla M., Williams J. P., Wilner D. J., 1996, *ApJ*, **465**, L133
- Neupane S., Garay G., Contreras Y., Guzmán A. E., Rodríguez L. F., 2020, *ApJ*, **890**, 76
- Ntormousi E., Hennebelle P., 2019, *A&A*, **625**, A82
- Olguin F. A., et al., 2021, *ApJ*, **909**, 199
- Olguin F. A., Sanhueza P., Ginsburg A., Chen H.-R. V., Zhang Q., Li S., Lu X., Sakai T., 2022, *ApJ*, **929**, 68
- Olguin F. A., et al., 2026, *ApJ*, **999**, 106
- Pagani L., Daniel F., Dubernet M.-L., 2009, *A&A*, **494**, 719
- Palau A., et al., 2014, *ApJ*, **785**, 42
- Peretto N., Hennebelle P., André P., 2007, *A&A*, **464**, 983
- Peretto N., et al., 2013, *A&A*, **555**, A112
- Peretto N., Rigby A. J., Louvet F., Fuller G. A., Traficante A., Gaudel M., 2023, *MNRAS*, **525**, 2935
- Pickett H. M., Poynter R. L., Cohen E. A., Delitsky M. L., Pearson J. C., Müller H. S. P., 1998, *J. Quant. Spectrosc. Radiative Transfer*, **60**, 883
- Qin S.-L., Schilke P., Wu J., Liu T., Wu Y., Sánchez-Monge Á., Liu Y., 2016, *MNRAS*, **456**, 2681
- Ragan S. E., Bergin E. A., Plume R., Gibson D. L., Wilner D. J., O'Brien S., Hails E., 2006, *ApJS*, **166**, 567
- Ramírez-Galeano L., Ballesteros-Paredes J., Smith R. J., Camacho V., Zamora-Avilés M., 2022, *MNRAS*, **515**, 2822
- Rygl K. L. J., Wyrowski F., Schuller F., Menten K. M., 2013, *A&A*, **549**, A5
- Schneider N., Csengeri T., Bontemps S., Motte F., Simon R., Hennebelle P., Federrath C., Klessen R., 2010, *A&A*, **520**, A49
- Schöier F. L., van der Tak F. F. S., van Dishoeck E. F., Black J. H., 2005, *A&A*, **432**, 369
- Shu F. H., 1977, *ApJ*, **214**, 488
- Singh A., et al., 2021, *ApJ*, **922**, 87
- Smith R. J., Shetty R., Stutz A. M., Klessen R. S., 2012, *ApJ*, **750**, 64
- Snell R. L., Loren R. B., 1977, *ApJ*, **211**, 122
- Traficante A., Fuller G. A., Smith R. J., Billot N., Duarte-Cabral A., Peretto N., Molinari S., Pineda J. E., 2018a, *MNRAS*, **473**, 4975
- Traficante A., et al., 2018b, *MNRAS*, **477**, 2220

Table A1. Measured line characterization parameters and their uncertainty for the central pixel of the observations.

$P_r = T_{\text{blue}}/T_{\text{red}}$	$v_{\text{sep}} = v_{\text{red}} - v_{\text{blue}}$	$w_{1/2}$ (km/s)	$D_r = T_{\text{dip}}/T_{\text{blue}}$ (km/s)
2.1 (0.3)	3.3 (0.1)	6.4 (0.1)	0.39 (0.06)

- Traficante A., Lee Y. N., Hennebelle P., Molinari S., Kauffmann J., Pillai T., 2018c, *A&A*, 619, L7
- Traficante A., Fuller G. A., Duarte-Cabral A., Elia D., Heyer M. H., Molinari S., Peretto N., Schisano E., 2020, *MNRAS*, 491, 4310
- Vázquez-Semadeni E., González-Samaniego A., Colín P., 2017, *MNRAS*, 467, 1313
- Vázquez-Semadeni E., Palau A., Ballesteros-Paredes J., Gómez G. C., Zamora-Avilés M., 2019, *MNRAS*, 490, 3061
- Walker C. K., Lada C. J., Young E. T., Maloney P. R., Wilking B. A., 1986, *ApJ*, 309, L47
- Walsh A. J., Bourke T. L., Myers P. C., 2006, *ApJ*, 637, 860
- Williams S. J., Fuller G. A., Sridharan T. K., 2005, *A&A*, 434, 257
- Williams J. P., Lee C. W., Myers P. C., 2006, *ApJ*, 636, 952
- Wu J., Evans Neal J. I., 2003, *ApJ*, 592, L79
- Wu J., Evans Neal J. I., Shirley Y. L., Knez C., 2010, *ApJS*, 188, 313
- Wyrowski F., et al., 2016, *A&A*, 585, A149
- Xie J.-J., et al., 2021a, *Research in Astronomy and Astrophysics*, 21, 208
- Xie J., et al., 2021b, *Science China Physics, Mechanics, and Astronomy*, 64, 279511
- Xu F., Wang K., He Y., Wu J., Zhu L., Mardones D., 2023a, *ApJS*, 269, 38
- Xu F.-W., et al., 2023b, *MNRAS*, 520, 3259
- Yang Y., Chen X., Jiang Z., Chen Z., Yu S., Li J., 2023, *ApJ*, 955, 154
- Zapata L. A., Loinard L., Rodríguez L. F., Hernández-Hernández V., Takahashi S., Trejo A., Parise B., 2013, *ApJ*, 764, L14
- Zhou S., Evans Neal J. I., Koempe C., Walmsley C. M., 1993, *ApJ*, 404, 232
- Zuckerman B., Evans N. J. I., 1974, *ApJ*, 192, L149

APPENDIX A: LINE CHARACTERISATION

To evaluate the fitting of the modelling results to the observed profiles, we develop a method to parameterise the line profiles of infall features. There are four parameters that can be used to encapsulate the characteristic blue asymmetric line profile:

- (i) $P_r = T_{\text{blue}}/T_{\text{red}}$, the ratio of the peak temperature of the blue-shifted peak to the peak temperature of the red-shifted peak,
- (ii) $v_{\text{sep}} = v_{\text{red}} - v_{\text{blue}}$, the velocity separation of the two peaks,
- (iii) $w_{1/2}$, the full width of the line profile at half the peak intensity of the red side of the profile, which guarantees both the red and blue sides of the line are encompassed, and
- (iv) $D_r = T_{\text{dip}}/T_{\text{blue}}$, the ratio of the intensity at the minimum between the two peaks to the peak intensity of the blue-shifted peak.

Figure A1 displays these parameters on a typical infall profile. For our analysis, we selected the pixel in the observed data with the largest values of the parameter P_r . This pixel corresponds to the position $(l, b) = 335.5836^\circ, -0.2862^\circ$. The parameter values and their uncertainties measured for the observed central pixel are given in Table A1.

Figure 1 shows the spatial distribution of P_r , the ratio of the intensity of the blue-shifted peak to that of the red-shifted peak, across the SDC335. The map shows that the spectroscopic signature of infall is seen over a significant portion of the clump.

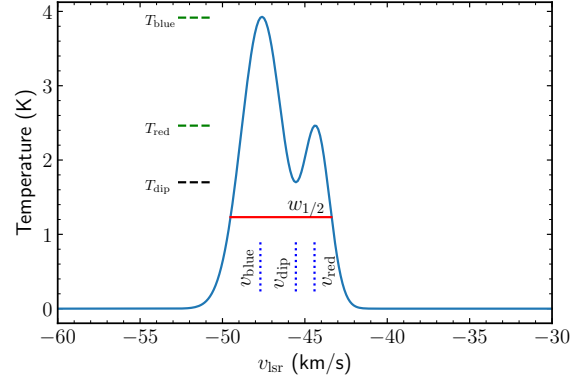


Figure A1. The characterisation of the line profile to quantify infall signatures. T_{blue} is the peak temperature of the blue side of the profile, while T_{red} is that of the red side. T_{dip} is the temperature at the absorption dip. v_{blue} and v_{red} are the corresponding velocities at the blue and red peaks, respectively. v_{dip} is the corresponding velocity at the absorption dip. $w_{1/2}$ is the full width of the line profile at half the peak intensity of the red side of the profile.

APPENDIX B: MODEL $V_C - \Delta v_b$ PLANES

Figure B1 shows the $v_c - \Delta v_b$ planes for the $p = 2$ LIME models (apart from model $M_{\text{LIME},7}$ which is shown in Fig. 10 in the main text).

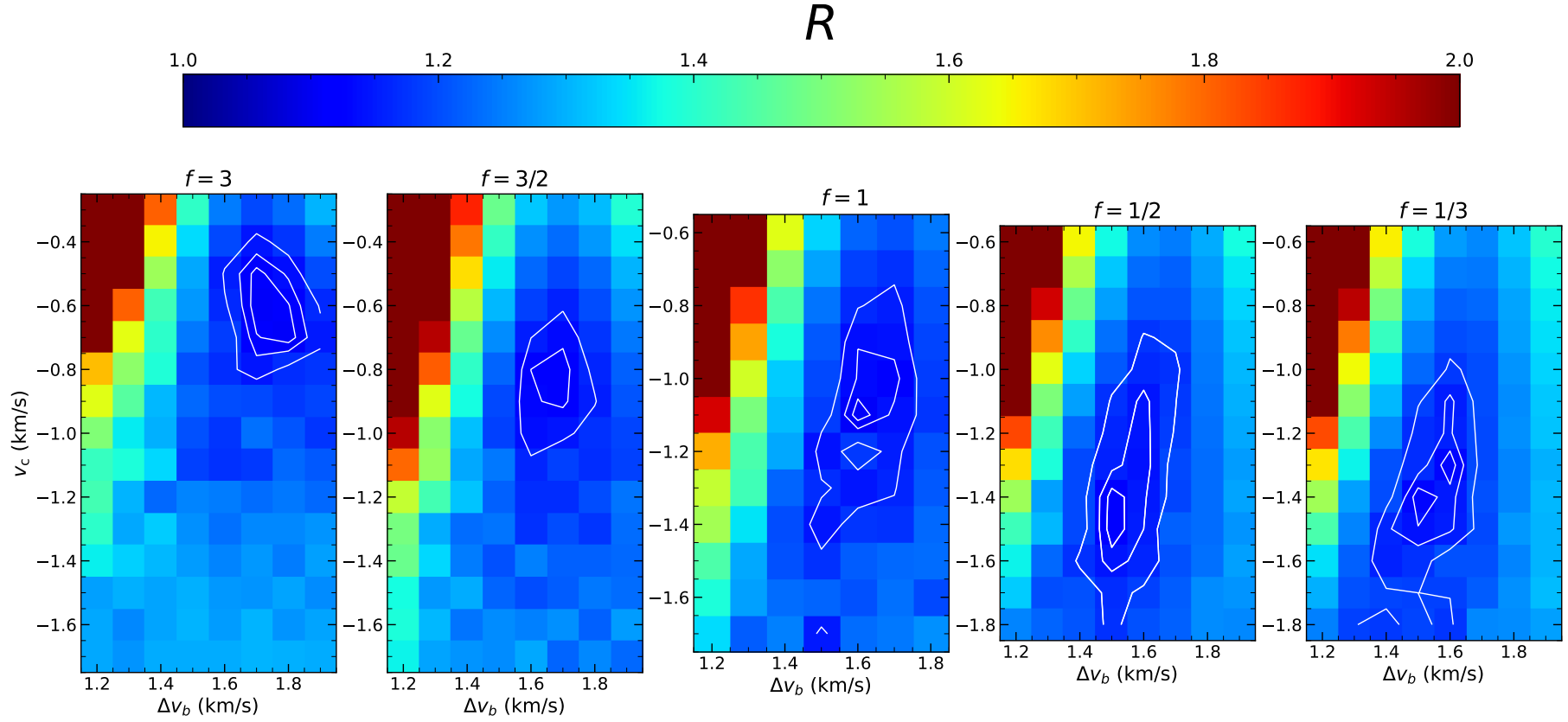


Figure B1. Colour scale images of the R parameter in $v_c - \Delta v_b$ plane for the central pixel of the observations. The axes show the full range of $v_{in,c}$ and Δv_b explored. Both values were sampled every 0.1 km s^{-1} . The panels show the $p = 2$ models with the f as labelled at the top of each panel. From left to right these are models $M_{LIME,10}$, $M_{LIME,9}$, $M_{LIME,6}$, $M_{LIME,5}$ and $M_{LIME,4}$. The contours show 1.01, 1.025 and 1.05 times the minimum R for the grid of models. From left to right this minimum value is 1.13, 1.12, 1.11, 1.10, 1.11.

This paper has been typeset from a \TeX/L\AA\TeX file prepared by the author.